Imaging and Analysis of Geological Porous Media

by

Riana Nicole Rivera

A thesis submitted to the Graduate Faculty of
Auburn University
in partial fulfillment of the
requirements for the Degree of
Master of Science

Auburn, Alabama
August 9, 2025

Keywords: Scanning Electron Microscopy, Pore structures, Carbon storage, Contrast agents, X-Ray CT

Approved by

Bryan S. Beckingham, Chair, Mary and John H. Sanders Associate Professor of Chemical Engineering
Lauren E. Beckingham, Co-chair, W. Allen and Martha Reed Associate Professor of Civil and Environmental Engineering
Steve R. Duke, Mary and John H. Sanders Associate Professor of Chemical Engineering

Abstract

Geological carbon sequestration (GCS) is a promising technology to remove CO_2 from the atmosphere. GCS is the process of capturing CO_2 from large point-sources or directly from the atmosphere, transporting the captured CO_2 to a storage site, and injecting it underground in geological formations for long-term storage. In this study, a calcareous dolomite sample obtained from Bartow County, Georgia was analyzed as a potential geological carbon sequestration site. Understanding carbonate rich minerals and their complex structures is crucial for predicting the impacts of dissolution and precipitation reactions when carbon dioxide is sequestered during carbon capture and storage. Here, scanning electron microscopy (SEM) imaging is utilized to obtain high resolution backscattered electron (BSE) images and energy dispersive spectroscopy (EDS) images of the sample's thin section. These images were used to create mineral maps. The mineral maps were then used to evaluate 2D sample characteristics such as porosity, pore connectivity, mineral abundances, and mineral accessibilities. Following mineral map analysis 3D x-ray computed tomography (XCT) images were obtained of the core sample. XCT images were used to extract larger 3D pore networks of the sample; however, XCT imaging cannot account for small-scale surface features. The BSE and EDS images used for analysis were then applied to the XCT images to allow for 2D and 3D image analysis of the core sample. This study aims to evaluate the mineral concentrations present around pore grain interfaces in carbonates by correlating 2D images with 3D images of two regions of a highly heterogeneous carbonate sample. In addition to imaging and analysis of mineral concentrations around pore structures in carbonates, this study also includes the development of an aqueous barium chloride contrast agent for enhanced XCT imaging of core samples. Two sets of XCT images were obtained to assess the viability of the contrast agent: one for a dry Bentheimer sandstone core, and one for the Bentheimer sandstone

core saturated with the aqueous barium chloride contrast agent. The captured XCT images were qualitatively processed, compared, and discussed.

Acknowledgments

This project is supported by the Southeast Regional CO_2 Utilization and Storage Acceleration Partnership (SECARB-USA) project funded by the U.S. Department of Energy and cost-sharing partners under grant number FE0031830, managed by the Southern States Energy Board.

I would like to thank Drs. Bryan and Lauren Beckingham for their constant support and guidance throughout my time in this program. Bryan and Lauren are truly great mentors who have challenged me to understand the why behind everything I learn and to approach challenges creatively. I am thankful for the opportunity to work under both of you, and I look forward to joining the Civil and Environmental Engineering PhD program in the Fall where I will be able to continue to learn from your expertise. I would also like to thank Dr. Duke for his guidance and career advice during my time in the program. Without the guidance and support of my committee members I would have given up on becoming an engineer months ago. Thank you all for supporting me and encouraging me to never give up.

I would also like to thank Carson, my parents, and my siblings for their constant support, patience, encouragement, and love. Thank you for always believing in me and encouraging me to be the best I can be. I couldn't have done it without you.

Lastly, I would like to thank my fellow WRISES and BPRG group members. Otis, Mitra, Nora, Nahian, Mohammad, Driba, Fahim, Zhuofan, Sam, Mark, Harrish, John, Logan, Sarah, Pravin, Yi-hung, and Adam, thank you all for your support and kindness. I am grateful to have had the opportunity to work alongside you all.

Table of Contents

List of Tables

List of Figures

List of Abbreviations

$BaCl_2$	Barium Chloride
BET	Brunauer-Emmett-Teller
BSE	Backscattered electron
CO_2	Carbon Dioxide
EDS	Energy dispersive spectroscopy
EOR	Enhanced oil recovery
GCS	Geological carbon sequestration
SEM	Scanning electron microscope
XCT	X-ray computed tomography
XRD	X-ray diffraction

Chapter 1. Introduction

1.1 Background

Burning of fossil fuels is an integral part of modern society due to its widespread usage in daily human activities. Fossil fuels are used in most sectors of society such as power, transportation, agriculture, industrial, and many more (Yoro & Daramola, 2020; Ritchie, 2020). While the impact to society has been positive, the increase of anthropogenic carbon dioxide (CO_2) in the atmosphere has raised climate change concerns (NAS, 2014).

Increased concentrations of CO_2 have had a noted effect on global temperatures. Greenhouse gases, such as CO_2, trap heat within the Earth's atmosphere which causes a rise in global temperatures, weather pattern changes, rising sea levels, and ocean acidification, for example (Aizebeokhai, 2009; NAS, 2014). As concentrations of CO_2 in the atmosphere continue to rise, concerns for reducing the effects of the greenhouse gas effect have gained interest. This requires a global collaborative effort, such as the Paris Agreement. The Paris Agreement is a treaty designed to limit global warming to below 2°C above pre-industrial temperatures (Delbeke et al., 2019). Attaining this goal requires implementation of several greenhouse gas removal and reduction technologies as no one solution can limit global warming to below 2°C (ExxonMobil, 2024). Such approaches include improving energy efficiency, developing renewable energy sources, decarbonizing industries, and transitioning to sustainable transportation (Rosenfeld et al., 2000). Direct air capture, carbon mineralization, geological carbon sequestration, and bioenergy with carbon capture and storage are being considered as technologies to either remove existing CO_2 from the atmosphere or store captured/produced CO_2 (ICEF, 2018; Oldenburg et al., 2009).

1.2 Geologic Carbon Sequestration

Geological carbon sequestration (GCS) is a promising technology to remove CO_2 from the atmosphere. GCS is an engineered carbon storage method that mimics biological carbon sequestration, which occurs naturally in trees, soil, and water (Lal, 2008). GCS is the process of capturing CO_2, from large point-sources or directly from the atmosphere, transporting the captured CO_2 to a storage site, and injecting it underground in geological formations for long-term storage (IPCC, 2005; Lal, 2008). The geological formations used for GCS are typically exhausted oil fields or subsurface saline aquifers. The benefit of using exhausted oil fields for GCS is that it allows for enhanced oil recovery (EOR), while subsurface saline aquifers have the added benefits of potential mineralization and permanent trapping of the sequestered CO_2.

Gas injected EOR is utilized by oil companies to extend the life of exhausted oil fields. Gas injection uses gases such as natural gas, nitrogen, or CO_2 to push trapped oil to locations where it can be collected. CO_2 is of interest for this process because it can increase flow rate while lowering the oils viscosity (Blunt et al., 1993; Thomas, 2008; Duda et al., 2010). As of 2020, there are over 142 projects across the United States that have collectively injected over 1.6 billion cubic feet of CO_2 for EOR (Wallace, 2021).

Subsurface saline aquifers are of interest for GCS because of their ubiquity and large storage capacity (Bachu et al., 1993; Holloway, 1997). When CO_2 is sequestered into a deep subsurface aquifer, it dissolves and reacts with the brine present within the geologic formation. These reactions create carbonic acid, bicarbonate, and carbonate, which causes the fluid to become more acidic (Kaszuba et al., 2003; Oelkers et al., 2008). Overtime, these geochemical reactions can dissolve and precipitate minerals in the formation, which can change the formation's porosity and permeability by altering pore connectivity, shapes, and sizes (Algive et al., 2012; Beckingham et al., 2013; Nogues et al., 2013; Noiriel et al., 2016).

Understanding these characteristics is crucial for predicting how the geological formations porosity and permeability will be altered when subjected to the geochemical reactions associated with GCS (Zhang et al., 2015; Xu et al., 2017; Lopez Rivera & Beckingham, 2024). Porosity changes are straightforward while permeability changes are much more complex and difficult to predict. In general, mineral dissolution increases porosity while mineral precipitation decreases porosity. In terms of permeability, mineral dissolution and precipitation may alter key characteristics that control permeability such as pore connectivity (Nogues et al., 2013; Changneau et al., 2015; Steinwinder & Beckingham, 2019; Sabo & Beckingham, 2021).

1.3 Imaging Techniques

2D and 3D imaging techniques have been utilized to better understand characteristics of geologic samples such as porosity, pore size, pore connectivity, mineral abundances, mineral accessibilities, and many more (Anselmetti et al., 1998; Qin & Beckingham, 2019; Safari et al., 2021; Salek et al., 2022). Scanning electron microscopy (SEM) is a 2D imaging tool that can be utilized to obtain backscattered electron (BSE) and energy dispersive spectroscopy (EDS) images at the nanometer to micrometer scale of geologic porous media. BSE images provide high resolution visualization of pore structures, mineral textures, grain sizes and shapes, and pore-grain interface features (Beckingham et al., 2017; Saif et al., 2017; Lyu et al., 2019; Qin & Beckingham, 2019; Salek et al., 2022). EDS images provide elemental composition data. BSE and EDS images can be paired together to identify minerals that are difficult to see in other imaging techniques (Marmo et al., 2005; Li et al., 2021; Liu et al., 2021). Once identified, the quantification of mineral abundances and accessibilities is feasible (Peters, 2009; Landrot et al., 2012; Beckingham et al., 2016). SEM imaging can also be used to understand small scale 2D features, which in turn allows for better understanding of mineral dissolution and precipitation in geologic porous media. SEM

imaging has many advantages; however, this type of imaging of geologic porous media requires destructive sample preparation to prepare the polished thin section. Polished thin sections are prepared by cutting a sample from a drill core, grinding to a thickness of 30 microns, impregnating with epoxy, attaching to a glass slide, and polishing.

X-ray computed tomography (XCT) is a non-destructive 3D imaging tool that can be used to visualize the characteristics and recreate 3D networks of pore structures of core samples. XCT imaging is useful for identifying characteristics of porous media such as porosity, connectivity, size, and distribution throughout the sample (Wildenschild & Sheppard, 2013; Glatz et al., 2016; Li et al., 2019; Liu et al., 2023). XCT imaging also allows for visualization of 3D features of geologic samples that are missed during 2D imaging techniques (Cnudde et al., 2011; Beckingham et al., 2013; Alatrash & Velledits, 2024; Asadi et al., 2024). Recreation of these characteristics can be useful for evaluating storage capacity and predicting geochemical reactions. While XCT imaging has the advantage of non-destructive sample preparation, it cannot provide information about sample mineralogy.

1.4 Imaging and Analysis of Porous Media

In this work, geologic porous media will be imaged and analyzed through use of 2D SEM and 3D XCT imaging techniques. In chapter 2, 2D SEM imaging will be utilized to obtain high resolution BSE and EDS images of a highly heterogeneous carbonate sample to quantify properties such as porosity, mineral abundance, and mineral accessibility. XCT imaging will be used to extract 3D pore networks of the carbonate that are missed during 2D imaging. The BSE and EDS images will then be applied to the XCT images to quantify mineral accessible surface areas. In chapter 3, a contrast agent will be developed and utilized to assess the viability of enhancing small scale features such as mineral textures and changes in surface topology that are typically

unobservable through XCT imaging. The goal of this work is to quantify accessible mineral surface areas in a carbonate sample obtained from Cassville, GA and provide an improved method for 3D XCT imaging.

1.5 Cassville, GA Site

The site analyzed in Chapter 2 of this work is Cassville Well 1 located in Bartow County, Georgia. Cassville Well 1 is a stratigraphic test well located in the northwest region of Georgia, near Plant Bowen, a coal fired power plant. Bartow County was selected as a GCS location of interest due to its proximity to industrial sources, porous reservoir, and impermeable caprock (Riestenberg et al., 2022). The general location of this stratigraphic test well can be seen as Point A in Figure 1.1.

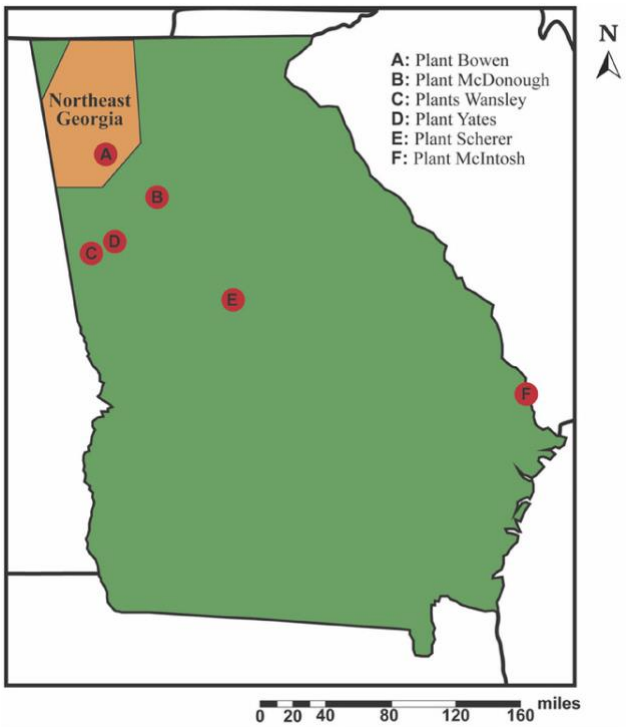

Figure 1.1. Cassville Well 1 location reproduced from Rivera & Beckingham (2025).

The well reached a total depth of 6,030 feet, with nine samples collected from various depths ranging between 3,508.01 ft to 3,894.02 ft. Of the nine samples collected from Cassville Well 1,

seven samples are dolomite, one sample is sandstone, and one sample is gypsum. Chapter 2 of this work focuses on the calcareous dolomite sample, Sample 15, which was collected from a depth of 3,745.94 feet.

1.6 Imaging and Analysis of Mineral Concentrations Around Pore Structures in Carbonates

Understanding mineral accessibilities is crucial for predicting where mineral dissolution and precipitation reactions will occur in geologic samples when CO_2 is sequestered. Many studies have explored the mineral accessibilities of sandstones through imaging techniques (Peters, 2009; Landrot et al., 2012; Beckingham et al., 2017; Qin & Beckingham, 2019; Salek et al., 2022). Mineral maps created by using BSE and EDS images revealed clay coatings and small-scale pore connectivity that affected the mineral accessibilities. While these studies are insightful, these observations maybe very different in carbonate samples.

Here, SEM imaging is utilized to obtain high resolution BSE and EDS images of the polished thin section of the calcareous dolomite sample collected from Cassville Well 1. BSE and EDS images were collected for two regions with differing porosity and mineral compositions. The collected images were used to create mineral maps. The mineral maps were then used to evaluate 2D sample characteristics such as porosity, pore connectivity, mineral abundances, and mineral accessibilities. Following mineral map analysis XCT images were obtained of the core sample. XCT images were collected for two regions with similar properties and features as the two regions selected during SEM imaging. XCT images were used to extract larger 3D pore networks of the sample; however, XCT imaging cannot account for small-scale surface features. The BSE and EDS images used for analysis were then applied to the XCT images to allow for 2D and 3D image analysis of the two regions of the core sample. This study aims to evaluate the minerals present

around pore grain interfaces in carbonates by correlating 2D images with 3D images of a highly heterogeneous carbonate sample.

This study aims to answer the following research questions:

- *What minerals are present along the pore grain interface within carbonates?*
- *Which mineral has the highest concentration along the pore grain interface within carbonates?*
- *Will large and small pore structures show similar mineral presence?*

1.7 Development of Contrast Agents for Enhanced 3D X-Ray Computed Tomography Imaging of Core Samples

XCT imaging of geologic porous media with contrast agents may be a promising means of enhancing characterization of pore structures and mineral textures without the use of traditional petrographic imaging techniques that require destructive sample preparation. Previous studies have successfully explored contrast agents such as saturated cesium chloride, potassium iodide solutions, and xenon gas for XCT imaging of geologic samples (Andrew et al., 2014; Mayo et al., 2015; Kuva et al., 2017). While these studies show promising results these methods are time consuming and require complex experimental setups.

Here, we first evaluate the potential XCT attenuation theoretically in order to identify a promising candidate for experimental investigation. From this evaluation an aqueous barium chloride ($BaCl_2$) solution was chosen and used as a contrast agent in XCT imaging to enhance characterization of a sandstone core. This study seeks to answer the question of whether the addition of aqueous $BaCl_2$ sufficiently alters the x-ray attenuation of pores and enhances small scale features such as mineral textures and changes in surface topology. The first set of XCT images were collected for the dry sandstone core, the second set using the same sandstone core,

but with the addition of the $BaCl_2$ solution. The XCT images were qualitatively processed and compared.

This study aims to answer the following research questions:

- *Will the addition of an aqueous barium chloride solution change the x-ray attenuation of pores?*
- *Is an aqueous barium chloride solution promising for deeper understanding of porous media properties?*

Chapter 2. Imaging and Analysis of Mineral Concentrations Around Pore Structures in Carbonates

2.1 Introduction

Carbonate reservoirs are of interest for geologic carbon sequestration (GCS) because of their ubiquity and large storage capacity (Ahr, 2011; Siqueria et al., 2017; Li et al., 2018). However, carbonates are highly heterogeneous with complex microscopic pore structures (Luquot & Gouze, 2009; Smith et al., 2013 and 2017; Gang et al., 2025). Due to the complex microscopic pore structures and highly heterogeneous nature of carbonate reservoirs it is still challenging to accurately quantify and characterize mineral properties such as abundance, accessibility, and accessible surface area.

Accurate quantification and characterization of host formations for GCS is important because CO_2 sequestration can cause geochemical reactions (Zhang et al., 2015; Dai et al., 2020; Lopez Rivera & Beckingham, 2024). The geochemical reactions associated with GCS can cause mineral dissolution and precipitation, which can ultimately alter the formations pore characteristics such as connectivity, shapes, and sizes (Beckingham et al., 2013; Jun et al., 2013; Stack, 2015; Noiriel et al., 2016). Without accurate characterization of the already complex microscopic pore structures within carbonates, the flow and transport of the sequestered CO_2 cannot be accurately predicted. Thus, it is necessary to understand which minerals are present around pore grain interfaces and at what abundance to better predict the pore alterations that will occur with the mineral dissolution and precipitation reactions (Kaszuba et al., 2013; Noiriel & Daval, 2017; Seigneur et al., 2019).

Imaging of geologic porous media has gained interest as a method to provide insights on pore and mineral characteristics. 2D imaging tools such as scanning electron microscopy (SEM) can be

used to obtain high resolution backscattered electron (BSE) and energy dispersive spectroscopy (EDS) images. BSE images can provide visualization of pore structures, mineral textures, grain shapes and sizes, and pore-grain interface features at the nanometer to micrometer scale, while EDS images provide elemental data (Beckingham et al., 2017; Saif et al., 2017; Lyu et al., 2019; Qin & Beckingham, 2019; Salek et al., 2022). When BSE and EDS images are paired together, they can be used to create mineral maps. Mineral maps can then provide unique and valuable information about mineral abundance and accessibility. However, 2D imaging cannot account for 3D features within samples. To overcome this limitation, x-ray computed tomography (XCT) has been used to extract 3D information about porous media such as pore networks, pore connectivity, and pore size distribution (Wildenschild & Sheppard, 2013; Glatz et al., 2016; Li et al., 2019; Liu et al., 2023).

Use of 2D and 3D imaging techniques may be a promising means of understanding characteristics of porous media. Landrot et al. (2012) developed a new 2D and 3D imaging approach that allowed for the characterization of reactive mineral surface areas within porous media. Beckingham et al. (2017) expanded on the approach developed by Landrot et al. (2012) by quantifying the mineral surface areas within a volcanic sandstone prior to a flow through experiment that yielded significant improvement in predicted experimental results. Qin & Beckingham (2019) assessed the impact of image resolution on the quantification of mineral abundances and accessible surface areas of a sandstone sample. Salek et al. (2022) enhanced the understanding of mineral accessibility for seven sandstone samples with varying mineral compositions by comparing variations due to different pore connectivity approaches. While these studies provide unique and valuable insights into mineral properties such as abundance, accessibility, and accessible surface areas all samples utilized in these works were sandstones.

This study is the first effort to quantify accessible mineral surface areas in a carbonate sample by utilizing the 2D and 3D imaging analysis method developed by Landrot et al. (2012). Here, 2D BSE and EDS images will be obtained and analyzed for two regions close in proximity, but with varying characteristics within the highly heterogenous carbonate sample. The captured BSE and EDS images will be utilized to create and analyze mineral maps that will provide quantitative data about characteristics such as porosity, pore connectivity, mineral abundance, and mineral accessibility. 3D pore connectivity will be captured for both regions through XCT imaging. The 2D mineral maps will then be applied to the extracted 3D pore networks for both regions to obtain the accessible mineral surface areas. The results of this method will then be compared and discussed for both regions.

2.2 Materials and Methods

2.2.1 Sample Background and Preparation

A calcareous dolomite sample (Sample 15) obtained from Cassville Well 1 located in Bartow County, Georgia was selected for this work. Sample 15 was collected at a depth of 3,745.94 ft by Advanced Resources International. Figure 2.1 shows an optical image of the sample. X-ray diffraction (XRD) analysis was completed by Schlumberger Reservoir Laboratories located in Houston, Texas. XRD analysis (Table 2.1) indicates this sample is predominantly dolomite (51%) with subordinate amounts of calcite (19%), quartz (18%), K-feldspar (6%), and clay minerals (5%).

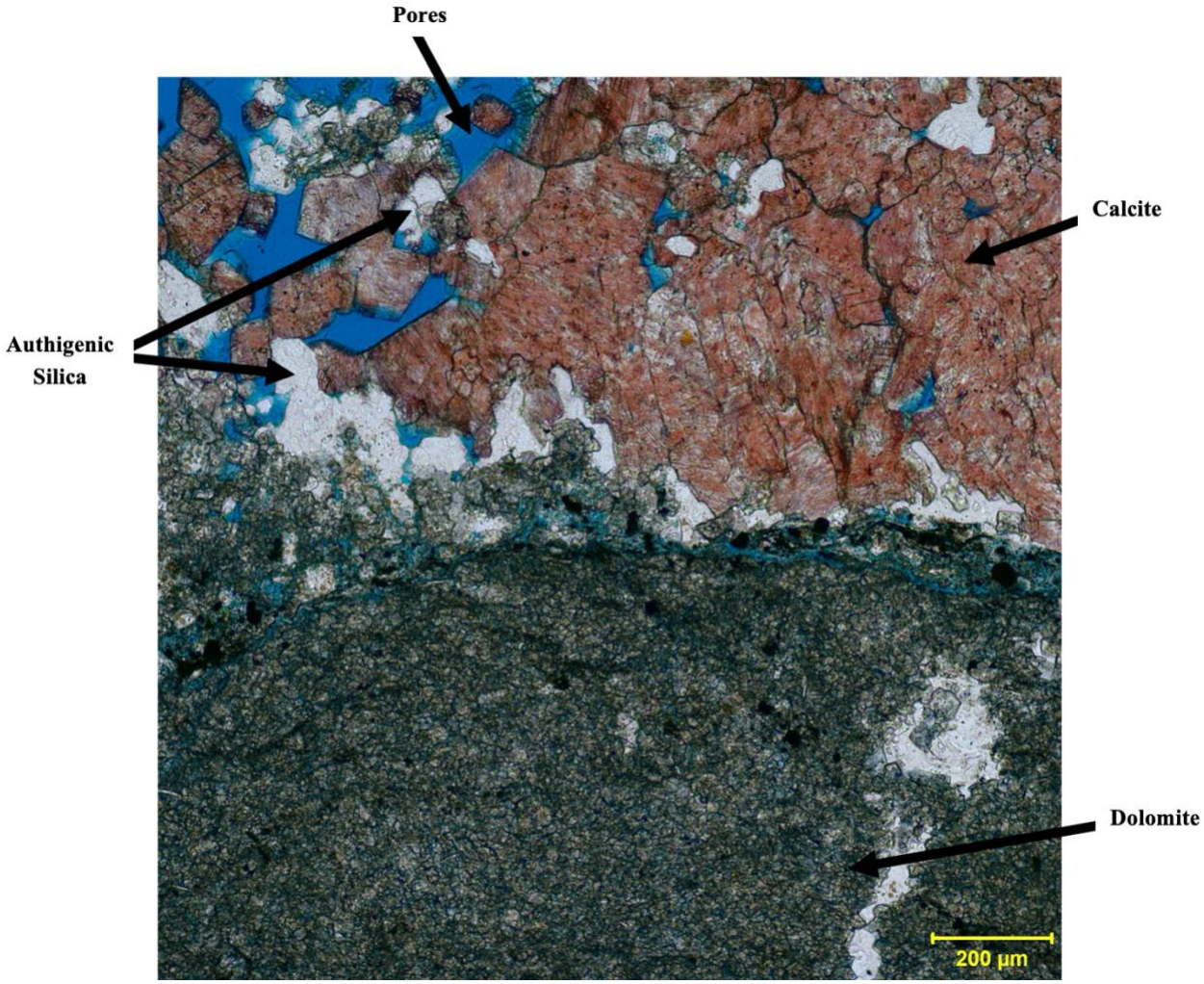

Figure 2.1. Optical microscope image of sample 15 (Schlumberger Reservoir Laboratories).

Table 2.1. Mineral composition of sample 15 from XRD analysis (wt%).

Sample number/ mineral	Dolomite	Calcite	Quartz	K-feldspar	Illite/Mica	Kaolinite	Pyrite
15	51	19	18	6	4	1	trace

In this work, thin section and core samples are considered. Thin section preparation was completed by Schlumberger Reservoir Laboratories. Preparation included epoxy impregnation, surface mounting to a thin section slide, and polishing. A Quorum Q150R ES Plus Sputter Coater at Auburn University was used to apply a gold coating to the thin section before Scanning Electron

Microscope (SEM) imaging. The core was a 1 inch length and 1 inch diameter sample and was used for 3D x-ray computed tomography (XCT) imaging.

2.2.2 Scanning Electron Microscopy

2.2.2.1 Image Acquisition

A ZEISS EVO-10 Scanning Electron Microscope (SEM) at Auburn University was used to obtain backscattered electron (BSE) and energy dispersive spectroscopy (EDS) images of the thin section. Under-high vacuum mode, a beam intensity of 20 kV and working distance of 8.28 mm were used to capture BSE images with a resolution of 590.9 nm. The BSE images were stitched together using the ImageJ plugin developed by Preibisch (2009). The BSE images covered an area of 65.5 mm^2 with 22,654 x 8,281 pixels, while EDS images covered two regions within the same field of view with resolutions of 820 nm and 1,021 x 798 pixels. EDS images were collected for Ca, Mg, Si, K, Al, Fe, and S in both regions.

2.2.2.2 Image Processing

2D SEM BSE and EDS images were used to evaluate various mineral properties such as porosity, mineral abundance, mineral accessibility, and pore connectivity. The BSE images were first manually thresholded using ImageJ to segment the pore and grain pixels. Porosity was calculated using a pixel counting code in the Matlab software.

Mineral identification was completed by following the approach used by Peters (2009). This method was challenging for the carbonate sample due to the similarities of pixel intensities in the BSE image for many minerals. Due to these challenges, the EDS images were heavily relied on to identify each mineral phase. Prior to mineral segmentation, ImageJ and Matlab were used to enhance the elemental images collected. ImageJ was used to register the BSE and EDS images.

Filters within ImageJ were also used to remove noisy pixels, while Matlab was used to remove small clusters of noisy pixels that were not removed during the ImageJ noise reduction process. The thresholded BSE images and the enhanced EDS images were then used to create segmented mineral maps. The segmented mineral maps were created by using a Matlab code, where each pixel was assigned a specific color to indicate a specific mineral phase.

Following mineral segmentation, mineral abundances and accessibilities were calculated for each of the different mineral phases in each of the two regions. The mineral abundances were determined by dividing the number of pixels for each mineral phase by the total number of mineral pixels. The mineral accessibilities were calculated by counting the number of pixels for each mineral phase adjacent to pore pixels and dividing this value by the total number of pixels adjacent to pore pixels. Here mineral accessibilities were calculated by assuming all pore pixels are accessible.

Mineral accessibilities were calculated by assuming all pore pixels are connected, however in reality not all pores are connected, therefore not all minerals adjacent to pore pixels are accessible. Pore connectivity can be affected by macro pores and nano pores. Nano pores are found in many clay minerals. In this work the sample contains two clay minerals, kaolinite and illite/mica. Previous work was done confirming the large connectivity of various clay minerals including kaolinite (Landrot et al., 2012; Beckingham et al., 2016). Based on these findings, this work assumed kaolinite and illite/mica have a large collection of connected nano pores and therefore contribute to the pore connectivity.

2.2.3 X-ray Computed Tomography

2.2.3.1 Image Acquisition

A Zeiss Xradia 620 Versa XCT at Auburn University was used to obtain 1010 x-y image slices over a 360° rotation of the core sample in two regions. A voltage of 140 kV and an exposure time of 2 seconds were used to capture both sets of images with voxel resolutions of 5.075 μm. From both sets of the 1010 captured images, 700 slices were selected for further analysis in this work. The extracted images for regions 1 and 2 were registered using the Zeiss Dragonfly software to ensure all images aligned seamlessly. The registered images were cropped into 3.55 mm x 3.55 mm squares with 700 x 700 pixels. The squares had total volumes of 44.74 mm^3. The images were then stacked to reconstruct the 3D images of both regions within the sample.

2.2.3.2 Image Processing

Prior to thresholding, the region 1 and 2 image stacks were filtered separately using the anisotropic diffusion filter in Zeiss Dragonfly. This was done to reduce noise within the images while preserving the edges of important features. The region 1 and 2 image stacks were then manually thresholded using Zeiss Dragonfly to separate the grain pixels from the pore pixels. This proved challenging due to the presence of small pores. Segmentation of the mineral and pore pixels was challenging around small pores due to edge effects. The porosities of the reconstructed 3D regions were then calculated by counting the grain and pore pixels of the thresholded image stacks using a pixel counter code in Matlab.

2D images are unable to account for 3D pore connectivity, so this work aims to calculate the mineral accessible surface areas following the work done by Landrot et al. (2012) and Beckingham et al. (2017). Mineral accessible surface areas for both regions were calculated by combining the mineral accessibility data from the 2D SEM images with the accessible mineral surface area data extracted from the 3D XCT images. The 3D XCT images have a total cross-sectional slice area of 12.60 mm^2, while the 2D BSE images of regions 1 and 2 only have areas of 6.87 mm^2 and 7.20

mm^2. Sub-cubes with total cross-sectional areas equivalent to the 2D BSE images were extracted from the larger XCT image stacks to ensure the 3D quantified mineral surface areas are comparable to the 2D SEM images. The sub-cubes for region 1 consisted of twenty adjacent 586 µm x 586 µm slices, while the sub-cubes for region 2 consisted of twenty adjacent 600 µm x 600 µm slices. The extracted sub-cubes for each region had the same surface area as the 2D BSE images for their respective regions. The extracted sub-cubes were selected due to having porosities and features similar to those observed in the regions 2D BSE images. This was done to ensure the representativeness of the selected cubes due to the high heterogeneity of the sample analyzed in this work. Thirty sub-cubes, fifteen from region 1 and fifteen from region 2, were created and analyzed using a Matlab code modified from Landrot (2012). The connected surface area in each sub-cube was identified and quantified by using the burning and marching algorithm within the modified Matlab code. The accessible surface area of each mineral was then calculated by multiplying the regions average connected surface area by the regions non-clay mineral accessibilities obtained from the 2D SEM images. Clay minerals were excluded from this calculation due to their nano connectivity and layered structures.

2.3 Results

2.3.1 Scanning Electron Microscopy

2.3.1.1 Image Acquisition and Thresholding

The captured BSE image with a resolution of 590.9 nm is shown in Figure 2.2. The two selected regions can be seen in Figures 2.3, 2.4a, and 2.5a. Region 1 covers an area of 6.87 mm^2 with 5,254 x 3,743 pixels, while region 2 covers an area of 7.20 mm^2 with 5,257 x 3,923 pixels. The BSE images were manually thresholded to separate pore and grain pixels to calculate sample porosity. The thresholded BSE images for regions 1 and 2 can be seen in Figures 2.4b and 2.5b, where grains

are shown in white and pore spaces are shown in black. The porosities for regions 1 and 2 were calculated to be 2.73% and 11.32%.

Figure 2.2. SEM BSE image of the sample thin section from Cassville Well 1.

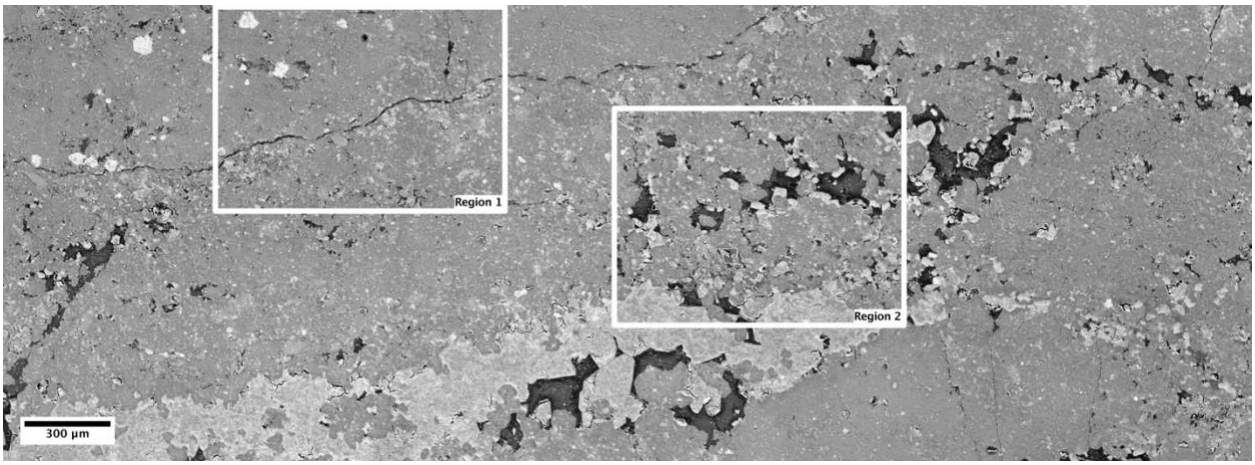

Figure 2.3. Locations of regions 1 and 2.

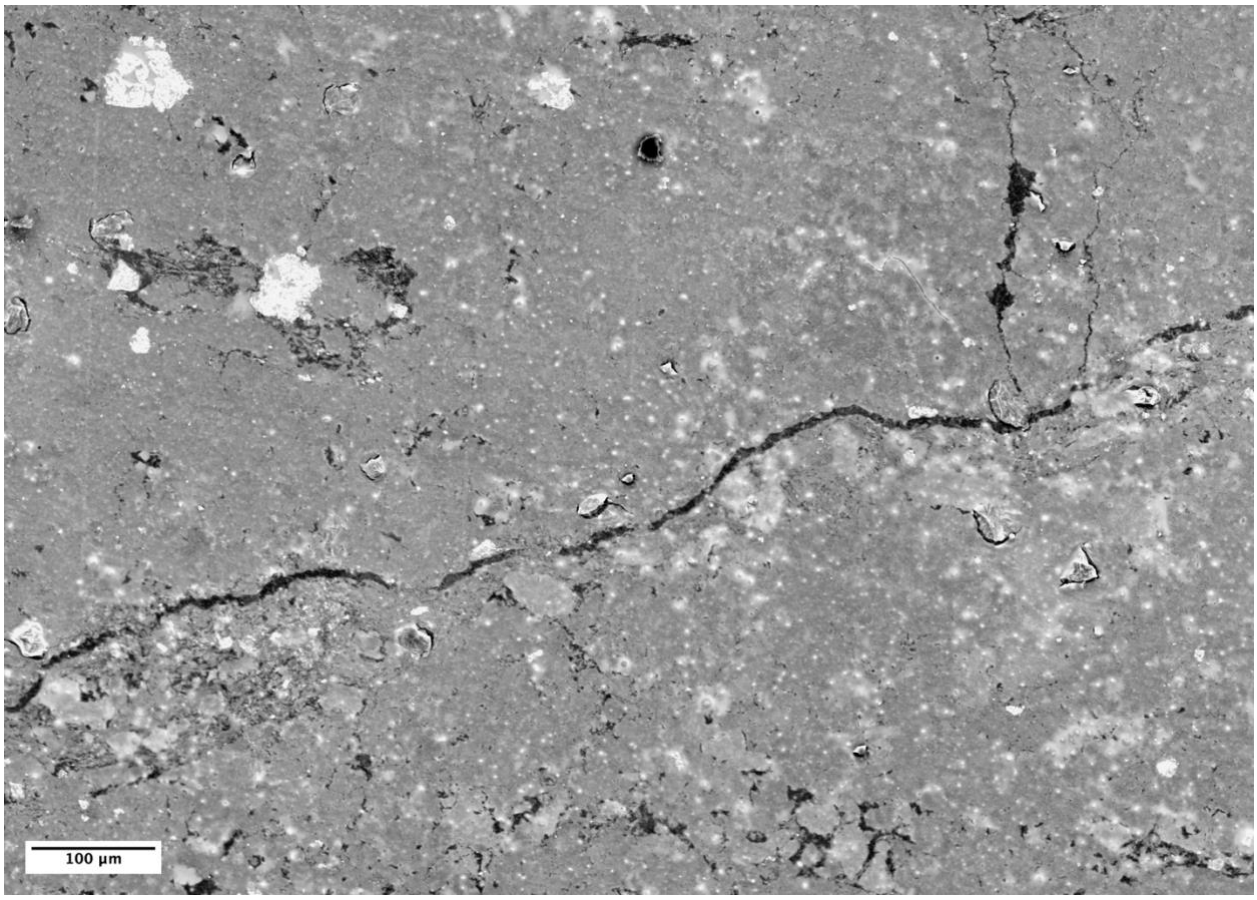

Figure 2.4a. BSE image of region 1.

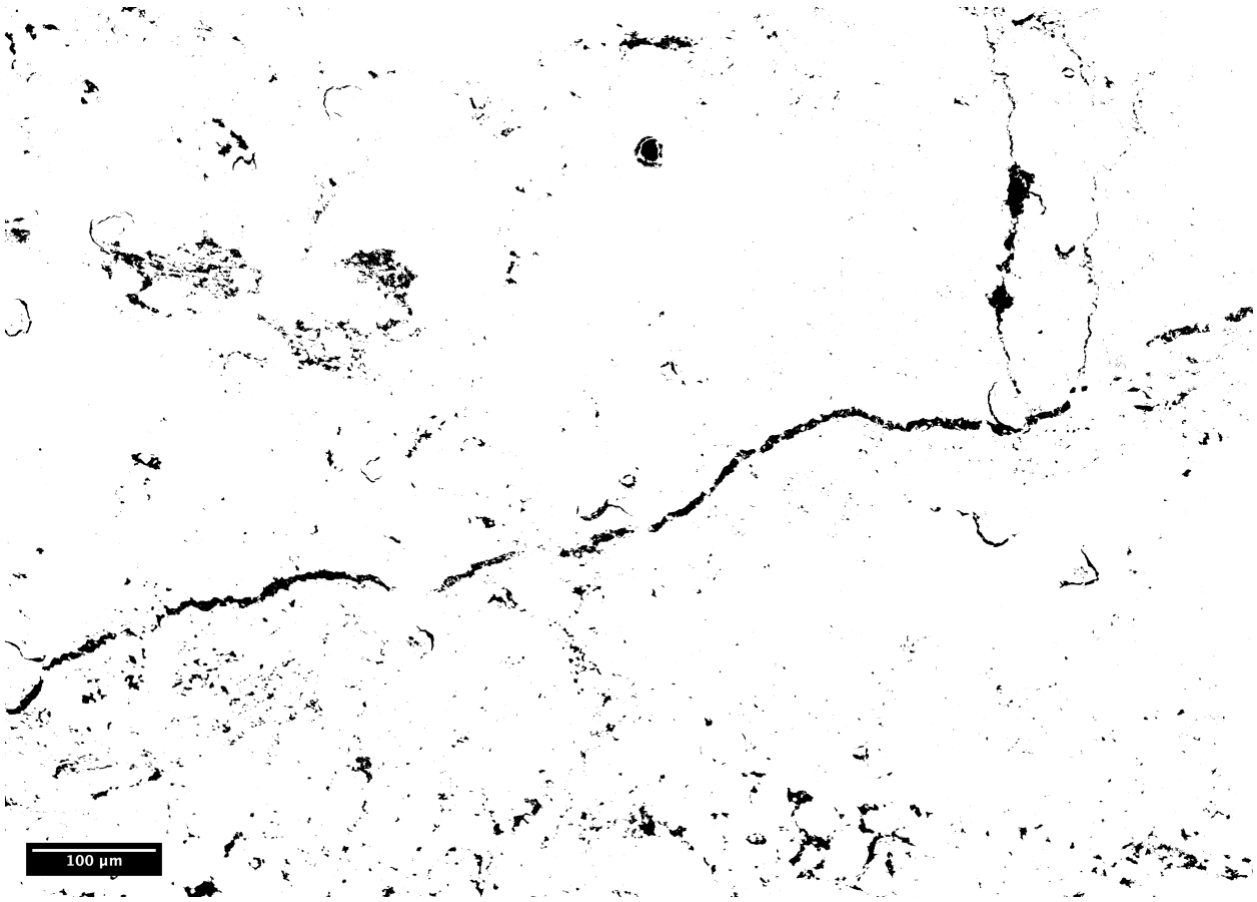

Figure 2.4b. Region 1 segmented image where grains are depicted in white and pores in black.

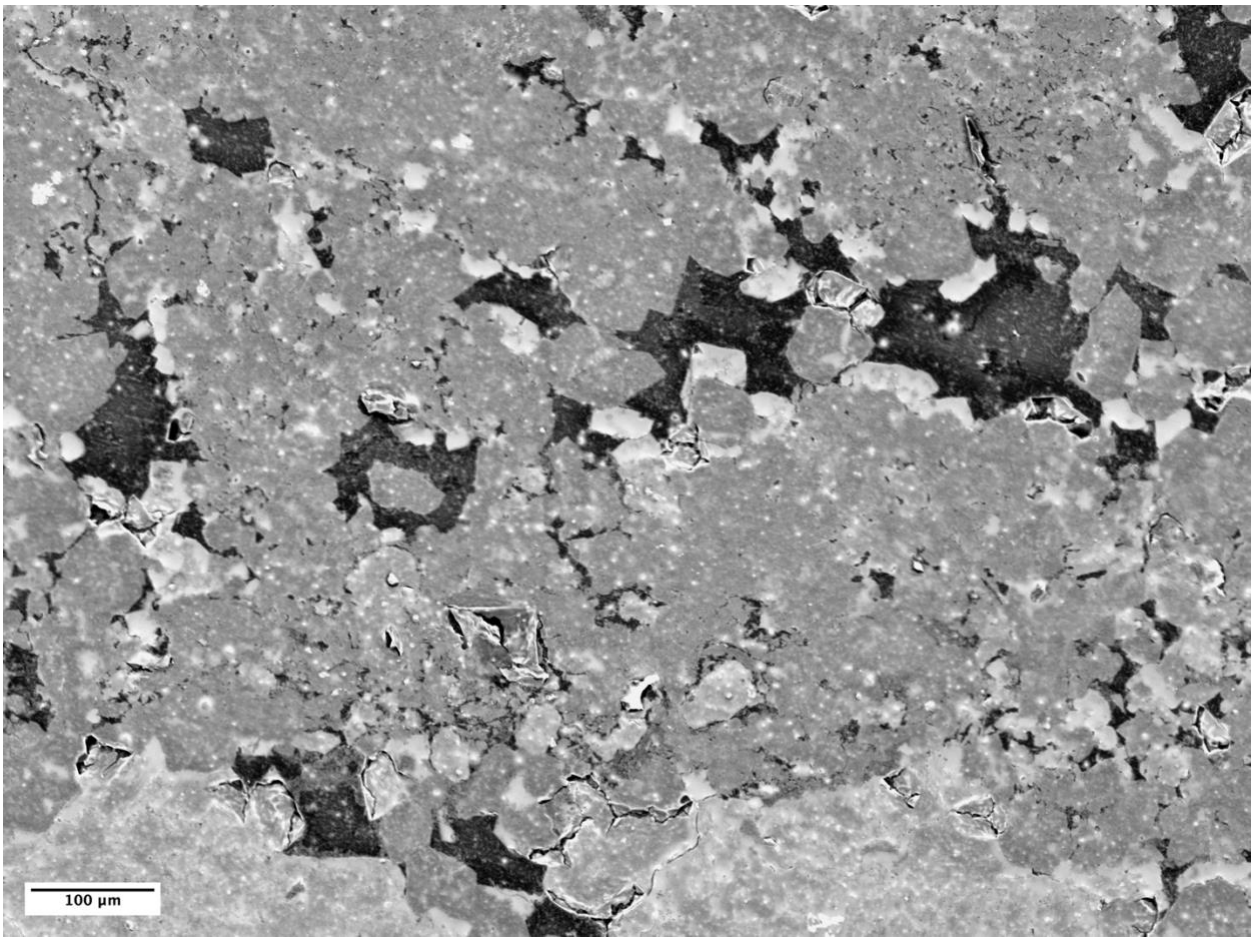

Figure 2.5a. BSE image of region 2.

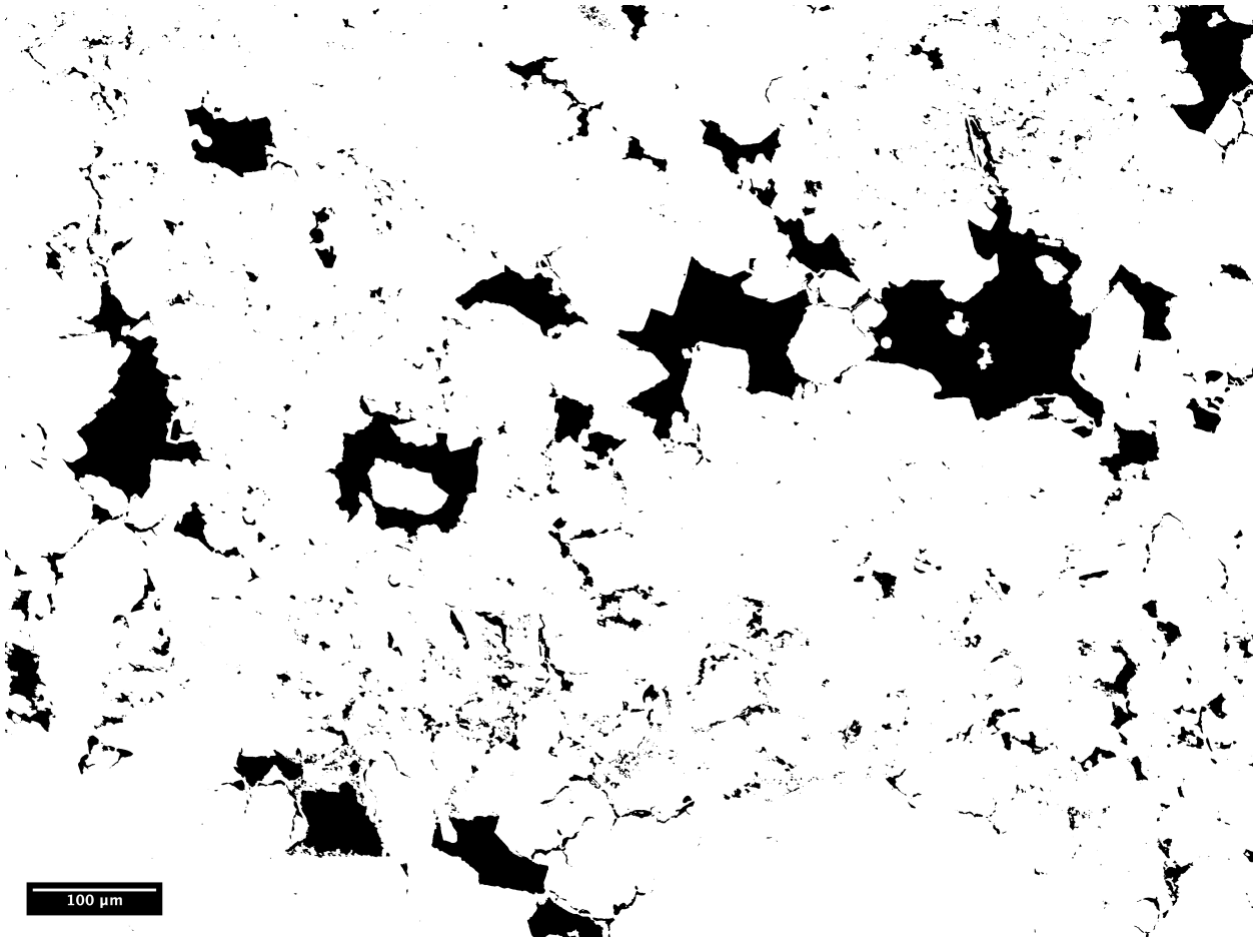

Figure 2.5b. Region 2 segmented image where grains are depicted in white and pores in black.

2.3.1.2 Mineral Identification and Quantification

EDS images for regions 1 and 2 can be found in Figures 2.6 and 2.7. Figures 2.8 and 2.9 show the segmentation of eight different mineral phases as demonstrated by the variation in BSE grey scale values and elemental identification by EDS images for regions 1 and 2. Each mineral phase is depicted in a different color. Segmentation by BSE grey scale values proved challenging due to many variations in grey scale values close together. EDS elemental images were largely relied on for mineral identification and quantification due to these challenges.

In this work, one of the eight identified mineral phases is labeled as an unknown mineral. The unknown mineral is observed where there is EDS elemental data present that conflicts with the rules set in the mineral map code. For example, if a pixel has EDS elemental data present for Mg, but not Ca the pixel will be labeled as unknown because it conflicts with the mineral map code rule that dolomite must have elemental data present for Ca and Mg.

Following mineral segmentation, mineral abundances were calculated for all eight mineral phases (Table 2.2). The mineral abundances were calculated by counting all of the various colored pixels and dividing each value by the total number of mineral pixels. Dolomite is the predominate mineral in this sample with an abundance of ~69v% in region 1 and of ~34v% in region 2. The unknown mineral phase was found to have an abundance of ~0.75v% in region 1 and of ~1v% in region 2.

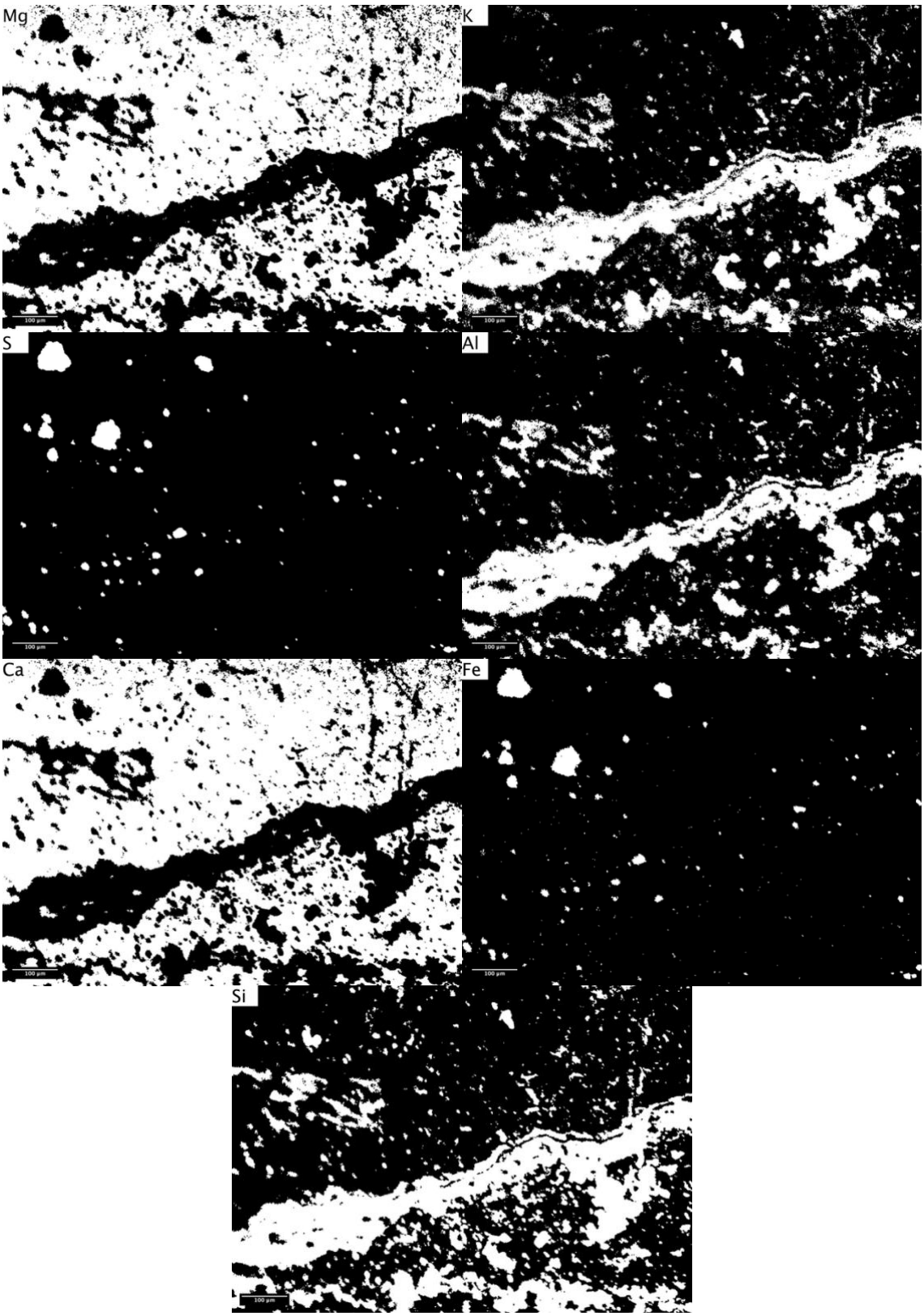

Figure 2.6. Segmented EDS images for region 1 with white pixels indicating elemental presence and black pixels indicating no elemental presence.

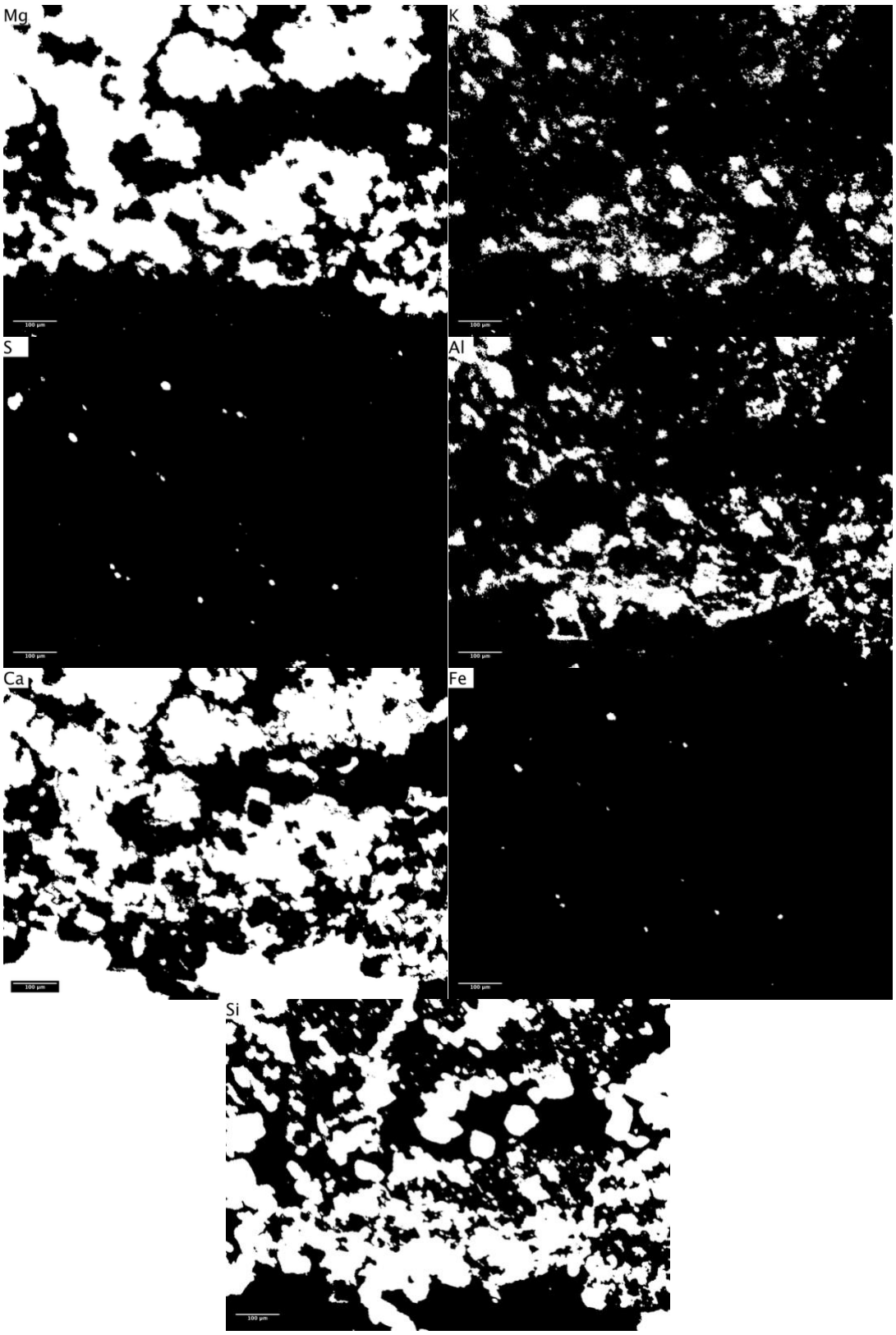

Figure 2.7. Segmented EDS images for region 2 with white pixels indicating elemental presence and black pixels indicating no elemental presence.

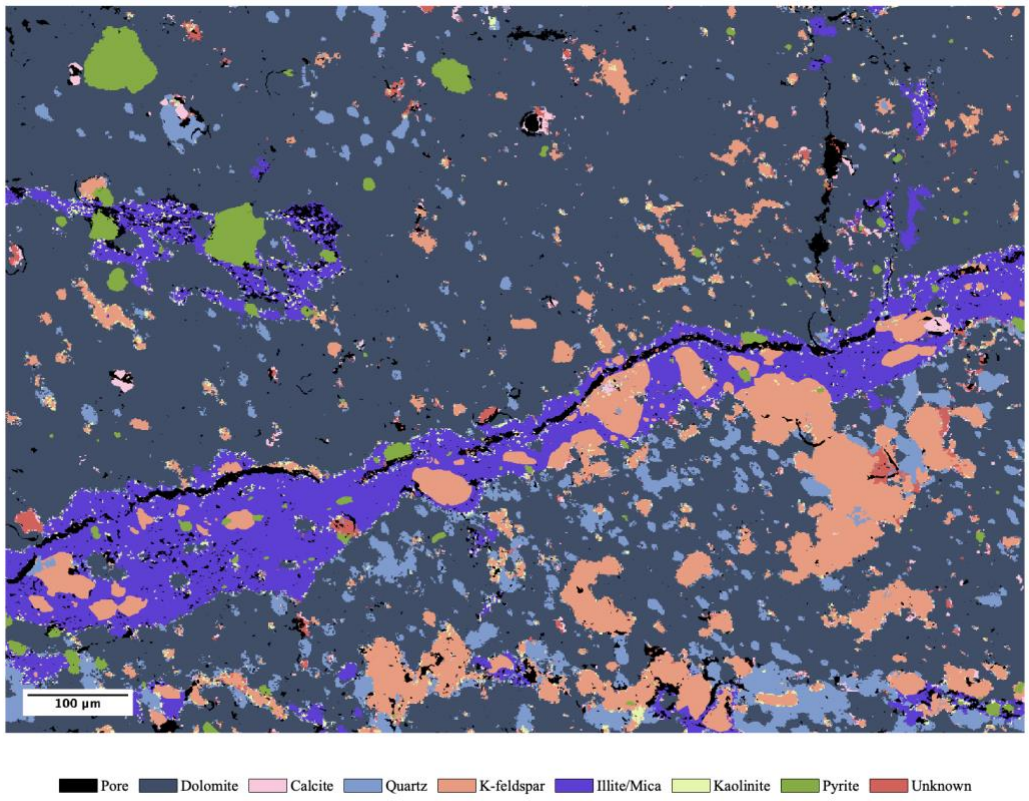

Figure 2.8. Segmented mineral map of the sample thin sections region 1.

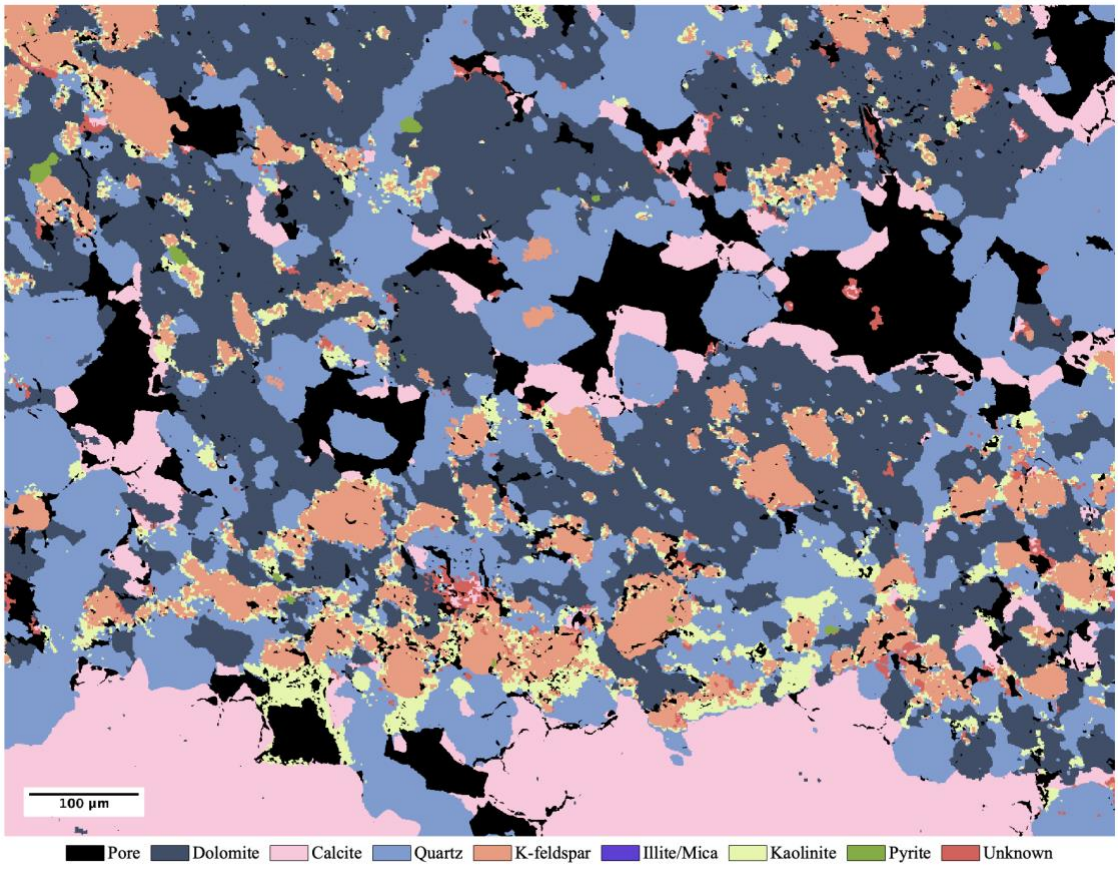

Figure 2.9. Segmented mineral map of the sample thin sections region 2.

Table 2.2. Mineral abundances (v%) and accessibilities (%) calculated from 2D segmented mineral maps.

Region	Minerals	Chemical formula	**A.** Abundance (v%)	**B.** Accessibility (all BSE pores) (%)	**C.** Accessibility (multi-scale pore connectivity) (%)
1	Dolomite	$CaMg(CO_3)_2$	68.88	34.67	14.29
	Calcite	$CaCO_3$	0.73	2.07	0.99
	Quartz	SiO_2	6.26	6.82	7.57
	K-feldspar	$KAlSi_3O$	9.53	9.56	9.31
	Illite/mica	$K_{0.6}(H_3O)_{0.4}Al_{1.3}Mg_{0.3}Fe^{2+}_{0.1}Si_{3.5}O_{10}(OH)_2 \bullet H_2O$	10.80	36.67	45.71
	Kaolinite	$Al_2Si_2O_5(OH)_4$	1.25	4.52	16.44
	Pyrite	FeS_2	1.80	1.71	3.50
	Unknown		0.75	3.98	2.18
2	Dolomite	$CaMg(CO_3)_2$	34.21	20.40	16.81
	Calcite	$CaCO_3$	17.79	20.38	21.56
	Quartz	SiO_2	30.41	24.06	30.50
	K-feldspar	$KAlSi_3O$	10.77	15.48	11.92
	Illite/mica	$K_{0.6}(H_3O)_{0.4}Al_{1.3}Mg_{0.3}Fe^{2+}_{0.1}Si_{3.5}O_{10}(OH)_2 \bullet H_2O$	0.0003	0	0
	Kaolinite	$Al_2Si_2O_5(OH)_4$	5.44	14.87	12.83
	Pyrite	FeS_2	0.18	0.03	0
	Unknown		1.20	4.79	6.38

2.3.1.3 2D Pore Connectivity

Pore connectivity is defined as the amount of pore pixels that are interconnected through macro or nano pores. Region 1 in Figure 2.8 appears to have an illite/mica vein that connects the left and right sides of the image. Region 2 in Figure 2.9 appears to have a high connected porosity, however after a closer look, it is apparent that many macro pores within the sample are unconnected due to pore-throat blockages caused by dolomite, calcite, and quartz.

Accessibilities based on multi-scale porosity were calculated by using a burning algorithm in Matlab (Landrot et al., 2012). This code started from each edge of the segmented mineral maps and worked its way in searching for pores connected through either nano pores within kaolinite and illite/mica or through macro pores. The code flipped all connected pores from black to white and all connected nanoporous kaolinite pixels from yellow to turquoise and all connected nanoporous illite/mica pixels from purple to teal. Following this procedure, the mineral accessibilities were recalculated by counting only mineral pixels adjacent to white pixels.

Figures 2.10 and 2.11 depict the connected pore space in white, while the unconnected pores remain in black. All connected nanoporous kaolinite pixels were flipped from yellow to turquoise, while all connected nanoporous illite/mica pixels were flipped from purple to teal. Table 2.3 shows the calculated porosity and connected porosity of both regions segmented mineral maps. The total porosity of region 1 was calculated to be 2.73%, while the connected porosity was calculated to be 1.53%. The total porosity for region 2 was calculated to be 11.32%, while the connected porosity was calculated to be 0.96%. In region 1, the connected porosity was affected by the pore-throat blockages caused by dolomite observed in the smaller fracture network seen in the upper right side of the image. In region 2, the connected porosity greatly decreased due to the pore-throat blockages by dolomite, calcite, and quartz.

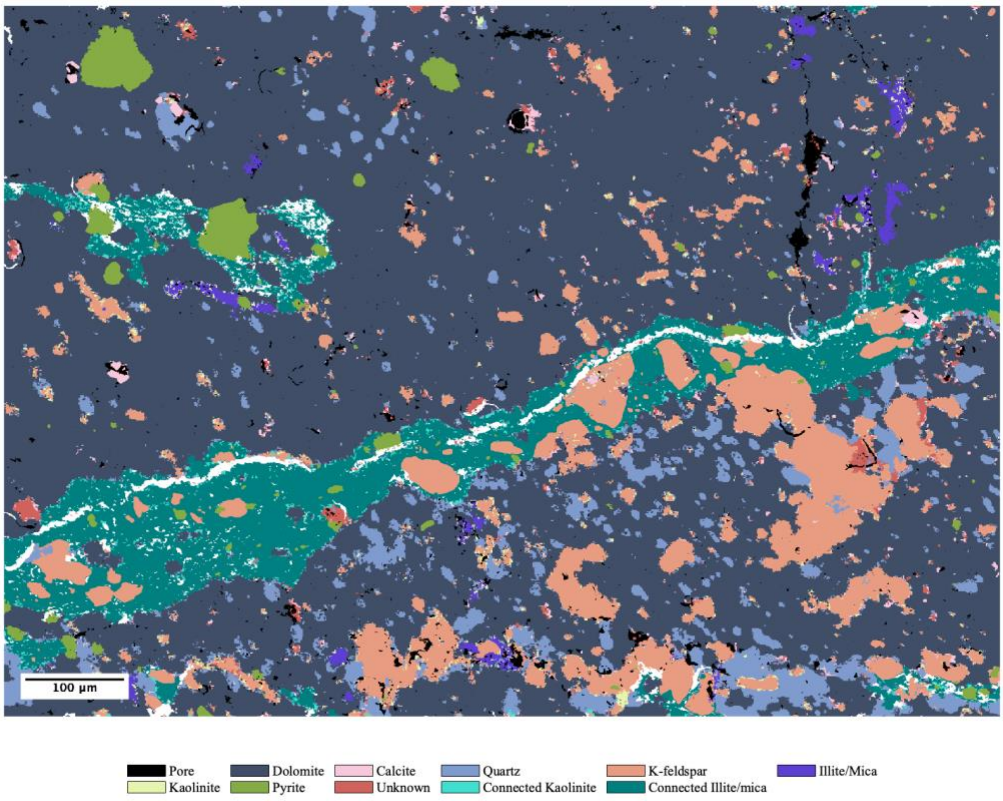

Figure 2.10. Region 1 connected porosity map of the segmented mineral map. Connected pores shown in white, while unconnected pores are shown in black.

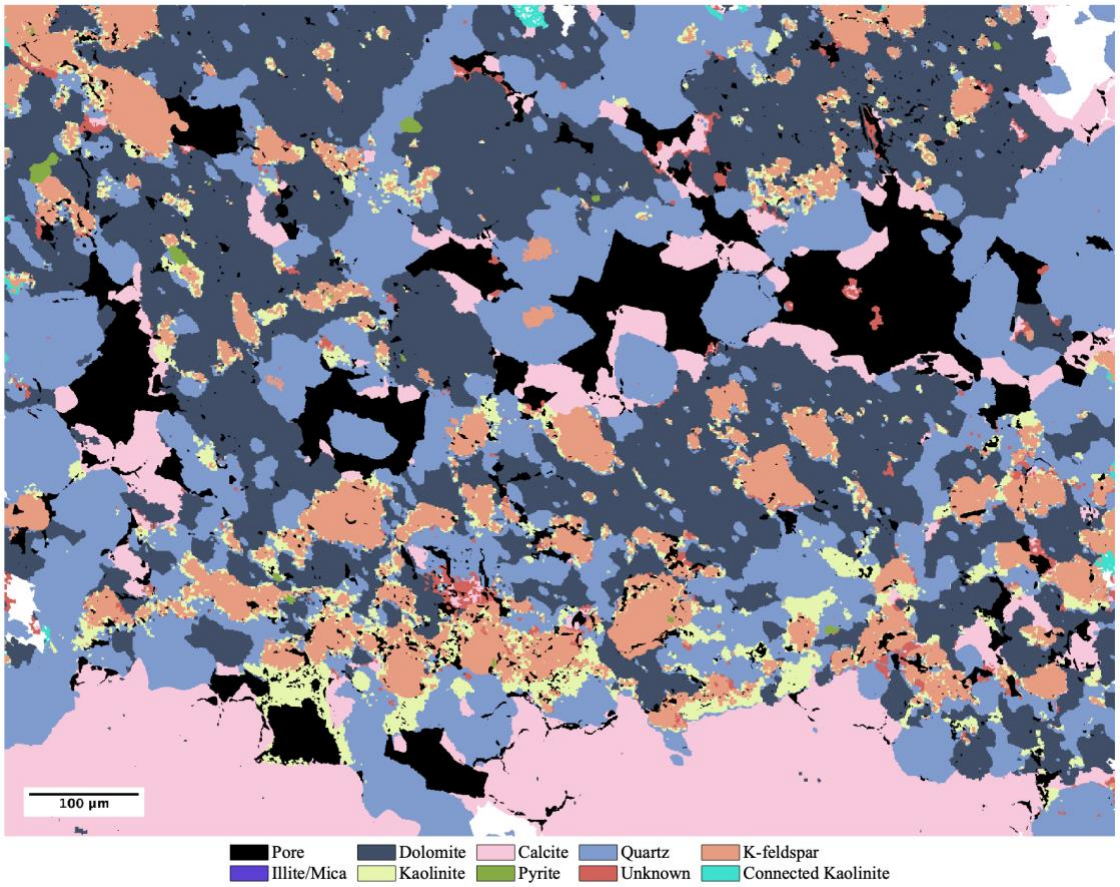

Figure 2.11. Region 2 connected porosity map of the segmented mineral map. Connected pores shown in white, while unconnected pores are shown in black.

Table 2.3. Calculated porosity (%) and connected porosity (%) of segmented images.

Region	Total Porosity	Connected Porosity
1	2.73	1.53
2	11.32	0.96

2.3.1.4 Mineral Accessibility

Accessible minerals are defined as mineral pixels that are beside pore pixels. The calculated mineral accessibilities can be found in Table 2.2. Accessibilities based on all BSE pores were calculated by counting each mineral phase pixel beside a pore pixel divided by the total number of pixels beside pore pixels. The values in column B of Table 2.2 do not include mineral accessibilities based on connectivity by nano porous minerals such as clay. It was calculated that 34.67% dolomite, 2.07% calcite, 6.82% quartz, 9.56% K-feldspar, 1.71% pyrite, 36.67% illite/mica, 4.52% kaolinite, and 3.98% of the unknown phase are accessible mineral pixels in region 1. It was calculated that 20.40% dolomite, 20.38% calcite, 24.06% quartz, 15.48% K-feldspar, 0.03% pyrite, 0% illite/mica, 14.87% kaolinite, and 4.79% of the unknown phase are accessible mineral pixels in region 2.

Accessibilities based on multi-scale porosity can be found in Table 2.2 column C. For region 1, it was calculated that 14.29% dolomite, 0.99% calcite, 7.57% quartz, 9.31% K-feldspar, 3.50% pyrite, 45.71% illite/mica, 16.44% kaolinite, and 2.18% of the unknown phase are accessible mineral pixels based on multi-scale porosity. For region 2, it was calculated that 16.81% dolomite, 21.56% calcite, 30.50% quartz, 11.92% K-feldspar, 0% pyrite, 0% illite/mica, 12.83% kaolinite, and 6.38% of the unknown phase are accessible mineral pixels based on multi-scale porosity.

2.3.2 X-ray Computed Tomography

2.3.2.1 Image Acquisition and Thresholding

The reconstructed XCT images of the core samples regions 1 and 2 can be found in Figures 2.12a and 2.13a. Figures 2.12b and 2.13b show the thresholded XCT images of the core samples regions 1 and 2 with pores in black and grains in white. The porosity for both regions of the core samples were calculated by counting the number or pore and grain pixels using a Matlab code.

The porosity calculated from the XCT images of region 1 was calculated to be 7.58%. This value is higher than the porosity of 2.73% calculated from the 2D SEM BSE image of region 1. This variation is believed to be due to the resolution of the XCT images being lower than that of the BSE image. With the resolution of the 3D XCT images being 5.075 μm and the resolution of the 2D BSE image being 590.9 nm, it is believed that the XCT images of region 1 lacked the resolution required to observe the tight pore spaces seen within the illie/mica vein. The porosity of the region 2 XCT images was calculated to be 10.24%. This value is slightly lower but agrees relatively well with the porosity of 11.33% calculated from the 2D SEM BSE image of region 2.

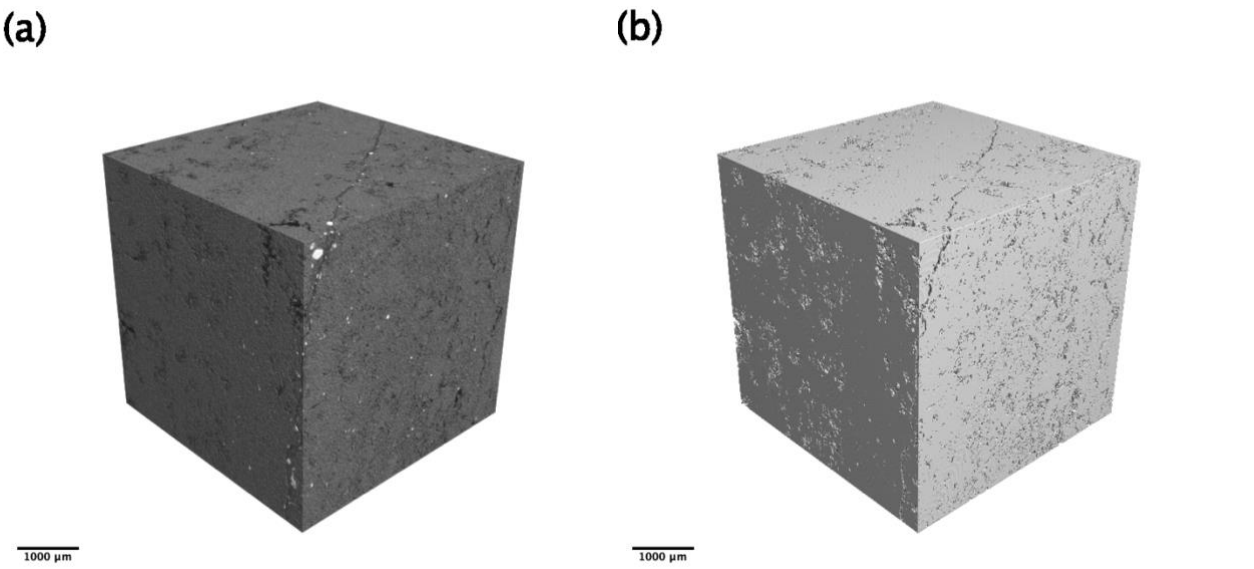

Figure 2.12. (a) Region 1 reconstructed 3D XCT image stack. **(b)** Region 1 thresholded 3D XCT image stack where grains are depicted in white and pores in black.

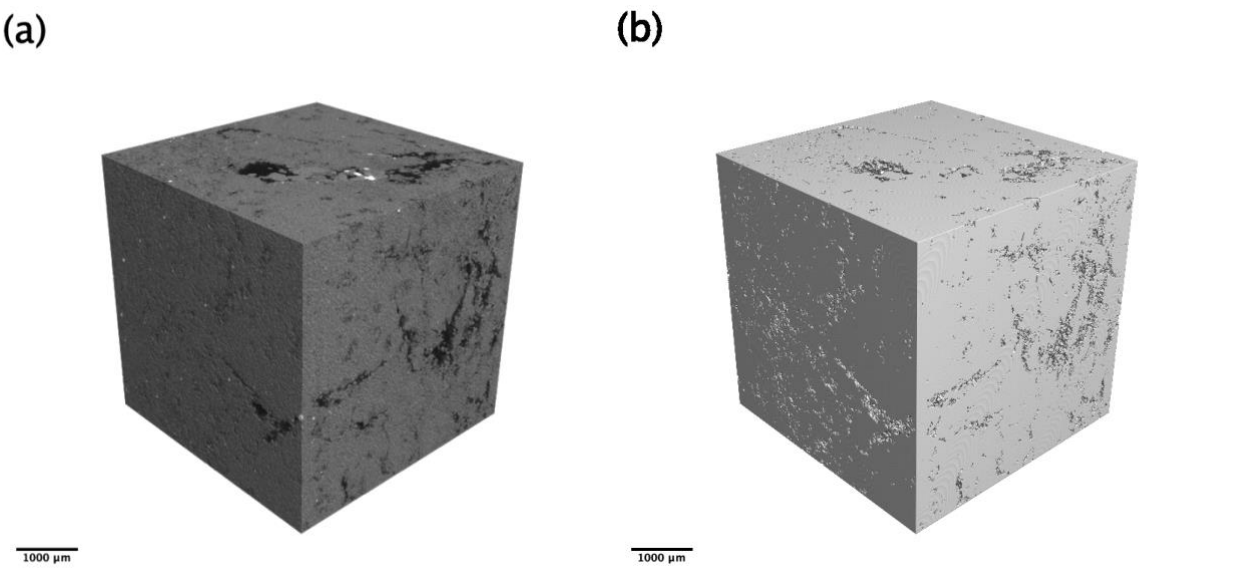

Figure 2.13. (a) Region 2 reconstructed 3D XCT image stack. **(b)** Region 2 thresholded 3D XCT image stack where grains are depicted in white and pores as black.

2.3.2.2 Accessible Surface Area

The accessible surface areas for both regions 1 and 2 were calculated using the 2D and 3D image correlation approach used by Landrot et al. (2012) and Beckingham et al. (2017). This approach is utilized to account for 3D pore connectivity that is missed in the 2D SEM images. The extracted sub-cubes from region 1 had an area of 586 x 586 μm^2 and a depth of 20 slices and the sub-cubes from region 2 had an area of 600 x 600 μm^2 and a depth of 20 slices. These volumes are 3D representations of the same total slice surface areas of 6.87 mm^2 observed in the region 1 BSE image and of 7.20 mm^2 observed in the region 2 BSE image. The average mineral bulk densities for both regions were calculated by using the obtained mineral percentages and the densities of each mineral phase. For region 1 the average mineral bulk density was calculated to be 2.79 g/cm^3, while the average mineral bulk density for region 2 was calculated to be 2.69 g/cm^3. The mass of individual sub-cubes was then calculated for both regions. The sub-cubes in region 1 each had a mass of 1.92 x 10^{-5} g and the sub-cubes in region 2 had a mass of 1.94 x 10^{-5} g. The average mineral

surface area for the fifteen sub-cubes extracted from region 1 was 0.024 m^2/g and the average total mineral surface area for the fifteen sub-cubes extracted from region 2 was 0.081 m^2/g.

Accessible mineral surface areas for all mineral phases except for the two clay minerals, kaolinite and illite/mica, and the unknown phase can be found in Table 2.4. Here, kaolinite and illite/mica were excluded due to this approach not accounting for the connectivity of clay minerals in the 3D XCT images. The accessible mineral surface areas were found by multiplying the regions average total mineral surface area by the region's accessibility of each mineral phase. The accessibility of each mineral phase used can be found in Table 2.2 columns B and C. Column A in Table 2.4 presents the data for the mineral accessible surface areas assuming all minerals adjacent to pore pixels are accessible. Column B in Table 2.4 presents the data for the mineral accessible surface areas accounting for multi-scale pore connectivity.

Table 2.4. Mineral accessible surface areas calculated from the accessibilities obtained from assuming all BSE pores are accessible and from accessibilities obtained from multi-scale pore connectivity.

Region	Minerals	Chemical formula	**A.** Accessible surface area (all BSE pores) (m^2/g)	**B.** Accessible surface area (multi-scale pore connectivity) (m^2/g)
1	Dolomite	$CaMg(CO_3)_2$	8.32×10^{-3}	3.43×10^{-3}
	Calcite	$CaCO_3$	4.97×10^{-4}	2.38×10^{-4}
	Quartz	SiO_2	1.64×10^{-3}	1.82×10^{-3}
	K-feldspar	$KAlSi_3O$	2.29×10^{-3}	2.23×10^{-3}
	Pyrite	FeS_2	4.10×10^{-4}	8.40×10^{-4}
2	Dolomite	$CaMg(CO_3)_2$	1.65×10^{-2}	1.36×10^{-2}
	Calcite	$CaCO_3$	1.65×10^{-2}	1.75×10^{-2}
	Quartz	SiO_2	1.95×10^{-2}	2.47×10^{-2}
	K-feldspar	$KAlSi_3O$	1.25×10^{-2}	9.66×10^{-3}
	Pyrite	FeS_2	3.88×10^{-3}	5.17×10^{-3}

2.4 Discussion

Porosities calculated from the segmented BSE and XCT images of both regions showed different trends. In region 1, the porosity obtained from the segmented BSE image was 2.73%, which was a lot smaller than the value of 7.58% obtained from the segmented XCT images. This discrepancy between porosities is believed to be due to the resolution of the XCT images not being high enough to obtain the fine details of the illite/mica vein that is observed. Region 2 presented similar porosity values of 11.33% (BSE obtained) and 10.24% (XCT obtained). The similarity between porosities in region 2 is likely due to the larger pores with less clay minerals present. When comparing both the porosities obtained from the BSE images for both regions, region 1 (2.73%) has a lot lower of porosity than region 2 (11.33%). However, when comparing the porosities obtained from the XCT images there is a smaller difference between regions 1 (7.58%) and 2 (10.24%).

Mineral abundance varied largely between the two regions, when comparing both regions, 1 and 2, certain conclusions can be made. In both regions dolomite is the mineral with the highest abundance. However, the abundance of dolomite in region 1 is 68.88v%, while in region 2 it is 34.21v% which is roughly two times the amount. In the region with a higher abundance of dolomite (region 1) the porosity is smaller (2.73%) while the region with a smaller abundance (region 2) has a larger porosity of 11.33%. Lower porosities calculated through this method indicate larger portions of the image is composed of mineral pixels. The observation of lower porosities and higher dolomite abundance through this method agrees well with the sample being predominantly composed of dolomite as revealed through XRD analysis. Further imaging of regions with different porosities needs to be conducted to verify the correlation between the higher abundances of dolomite and lower porosities.

The second most abundant mineral found in these samples differ. Illite/mica is the second most abundant mineral phase in region 1 at 10.80v% while quartz is the second most abundant mineral phase in region 2 at 30.41v%. After these two concentrations of minerals the abundance of other minerals slightly drops in both regions 1 and 2. With the next largest abundance in region 1 being K-feldspar at 9.53v%, and in region 2 calcite at 17.79v%. The region with lower porosity, region 1, presented larger mineral presence of illite/mica and K-feldspar while the region with higher porosity, region 2, presented larger amounts of quartz and calcite.

Segmentation of minerals with similar BSE pixel intensities proved challenging for the carbonate sample used in this work. Within region 1, the challenges faced were due to the low porosity and high consolidation of minerals with similar BSE pixel intensities. It is believed that discrepancies arose with proper mineral identification along the illite/mica vein and K-feldspar grain interfaces due to the large presence of clay minerals. Segmentation of region 2 proved less challenging due to the higher porosity and lower abundance of clay minerals present.

Mineral accessibility is correlated to the porosity of the samples. In turn, the accessibility of minerals in both regions differ. Region 1, having a smaller porosity of 2.73%, minimal minerals within the region may be accessed. Most minerals that can be accessed are focused on the linear vein that runs from right to left in the lower section of the image. This area is mostly comprised of accessible illite/mica (36.67%) and dolomite (34.67%) indicating that ~37% of the pore-grain interfacial pixels are comprised of illite/mica, while ~35% are dolomite. All other minerals within the region are less than 10% accessible. While in region 2, due to its porosity being 11.33%, most of the minerals found within the region may be accessed. The accessibility of quartz is 24.06%, dolomite 20.40%, calcite 20.38%, K-feldspar 15.48%, and kaolinite 14.87%. Mineral accessibility is a key characteristic for predicting and understanding the geochemical reactions associated with

GCS. Mineral accessibility indicates which minerals are along the pore-grain interface that will potentially be in contact with the reactive fluid when CO_2 is sequestered.

The mineral accessible surface areas were calculated from the accessibilities obtained from assuming all pores are connected and from the accessibilities obtained from multi-scale pore connectivity. When considering accessibilities obtained from assuming all pores are connected, region 1 presented dolomite as the mineral with the highest accessible surface area at 8.32×10^{-3} m^2/g followed by K-feldspar with an accessible surface area of 2.29×10^{-3} m^2/g. Region 2 presented similar accessibilities for quartz, dolomite, and calcite at 1.95×10^{-2} m^2/g, 1.65×10^{-2} m^2/g, and 1.65×10^{-2} m^2/g. The mineral with the least accessible surface area in both regions was pyrite with a surface area of 4.10×10^{-4} m^2/g in region 1 and of 3.88×10^{-3} m^2/g in region 2. The mineral accessible surface areas obtained here for region 1 do not agree well with the Braunauer-Emmett-Teller (BET) measured surface area values in literature. This is believed to be due to the large presence of clay found within region 1. However, the mineral accessible surface areas obtained for region 2 agree well with the low BET values within literature for quartz (2.25×10^{-2} m^2/g), calcite (1.39×10^{-2} m^2/g), and dolomite (1.40×10^{-3} m^2/g).

When considering accessibilities obtained from multi-scale pore connectivity, regions 1 and 2 presented different trends. Region 1 accessible surface areas based on multi-scale pore connectivity varied largely compared to the accessible surface areas assuming all pores are connected, except for K-feldspar which remained at a similar value of 2.23×10^{-3} m^2/g. Region 2 accessibilities calculated utilizing both methods remained relatively consistent showing only slight changes in accessible surface areas. The accessible surface areas for quartz, dolomite, and calcite in region 2 were calculated to be 2.47×10^{-2} m^2/g, 1.36×10^{-2} m^2/g, and 1.75×10^{-2} m^2/g. These differences are due to small amounts of overall pore connectivity captured in the regions.

Pore connectivity within both regions appears to follow a similar trend. In both regions the pore connectivity drastically drops, and both demonstrate a less than 2% connected porosity. In region 1, a drop from 2.73% to 1.53% is witnessed. The most accessible minerals due to the connected pores being illite/mica at 45.71% and dolomite at 14.29%. With region 2, a drop in porosity from 11.32% to 0.96% is witnessed. The most accessible mineral being quartz at 30.50%. Due to this dramatic drop in connectivity, not much can be gathered, and further data must be obtained from regions with larger pore connectivity. Typically, this method is used in sandstones that have a larger percentage of connected porosity. This is a limitation of this method while gathering data from these two regions and possibly for other carbonate samples with low connected porosities. In carbonates or other samples with low connected porosities, more accurate quantifications of mineral accessibilities may be achieved by considering all pores are connected due to the limited pore connectivity observed.

2.5 Conclusion

In this work, 2D and 3D imaging techniques are combined to gain a deeper understanding of how geologic porous media properties such as mineral abundance, mineral accessibility, and accessible surface area are impacted by region variation. Here, these properties were determined from a calcareous dolomite sample with 2D SEM and 3D XCT images collected from two different regions, a region with low porosity, region 1, and a region with high porosity, region 2. Understanding how regions with low and high porosities differ within the same sample is crucial for predicting how the geochemical reactions associated with CO_2 sequestration will alter the host formations pore characteristics such as connectivity, shapes, and sizes.

Here, the overall impact of region variation on mineral abundances, accessibility, and accessible surface area proves the need to characterize and understand how these characteristics

are distributed throughout carbonate samples. It was revealed that the region with low porosity, region 1, had more illite/mica and dolomite at the pore interfaces, while the region with high porosity, region 2, had more quartz, dolomite, and calcite at the pore interfaces. Further imaging is required to ensure that multiple regions with low and high porosities present similar trends to the two regions analyzed in this work. Without properly accounting for region variations when assessing and predicting the viability of a site for CO_2 sequestration discrepancies can occur when predicting mineral dissolution and precipitation reactions.

While this imaging analysis proved the importance of considering region variations when characterizing highly heterogeneous carbonate samples this method required additional time and cost requirements. Depending on the sample characteristics, grouping many regions with similar features may help reduce the large cost and time requirements while obtaining an accurate understanding of the characteristics of the sample of interest.

Chapter 3. Development of Contrast Agents for Enhanced 3D X-Ray Computed Tomography Imaging of Core Samples

3.1 Introduction

Geologic carbon sequestration (GCS) has gained interest as a method to reduce atmospheric CO_2 emissions. Injection of CO_2 into deep subsurface saline aquifers causes geochemical reactions that can dissolve and precipitate minerals within the host reservoir and caprock formations (Noiriel et al., 2004; Ketzer et al., 2009; de Silva et al., 2015). Such reactions can change the porosity and permeability of the formation by altering pore characteristics such as connectivity, shapes, and sizes (Algive et al., 2012; Beckingham et al., 2013; Nogues et al., 2013; Noiriel et al., 2016). It is necessary to understand these characteristics to predict how flow and transport within the geological formations will be changed when the geochemical reactions associated with GCS occur (Jun et al., 2013; Zhang et al., 2015; Dai et al., 2020; Lopez Rivera & Beckingham, 2024). Changes in porosity and permeability due to the mineral dissolution and precipitation reactions ultimately impacts the fate and transport of the CO_2 injected during GCS.

3D X-ray computed tomography (XCT) is a non-destructive imaging technique used to visualize the structures and characteristics of materials. XCT is an important tool used in many areas of research such as geology, soil and plant sciences, medicine, archeology, and many more (Asadi & Beckingham, 2021; Machado et al., 2019, 2023; Santos et al., 2020; Yin et al., 2023). XCT has proven highly valuable for characterization of geologic porous media (Wildenschild & Sheppard, 2013; Glatz et al., 2016; Li et al., 2019; Liu et al., 2023). In particular, pore characterization of geologic samples using XCT has gained a lot of interest because pore structures within cores can be studied without damaging the sample, in contrast to traditional petrographic imaging of thin sections.

While XCT imaging is beneficial because it is a non-destructive imaging technique, it cannot provide information about sample mineralogy or high-resolution details of small-scale features. Such data can be obtained from high-resolution 2D scanning electron microscopy (SEM) backscattered electron (BSE) and energy dispersive spectroscopy (EDS) images of geologic samples. BSE images provide high-resolution visualization of pore structures, mineral textures, grain sizes and shapes, pore-grain interface features, and a relative identification of minerals, while EDS images provide elemental composition data (Peters, 2009; Landrot et al., 2012; Beckingham et al., 2017; Li et al., 2021; Liu et al., 2021). Combined together, mineral phases can be identified in the collected images and mineral maps, depicting each mineral phase as a different color (as in Chapter 2). While SEM imaging provides unique and valuable information this type of imaging requires destructive sample preparation to prepare the polished sample required for image collection.

Use of contrast agents in XCT imaging of geologic porous media may be a promising means of enhancing characterization. Kuva et al. (2017) were able to successfully use a saturated cesium chloride solution as a contrast agent in XCT and SEM-EDS imaging of six crystalline rock samples to visualize connected porosity. Andrew et al. (2014) utilized a potassium iodine solution to measure the contact angles between immiscible fluids in a limestone sample. Mayo et al. (2015) accurately estimated the regions of connected and unconnected porosity in seven samples of varying composition and porosity by using xenon gas. While these studies show promising results, the method utilized by Kuva et al. (2017) was time consuming by requiring the samples to soak in the contrast fluid for 141-365 days, Andrew et al. (2014) faced the challenge of accurately identifying the fluid grain interfaces, and Mayo et al. (2015) required use of the synchrotron and a complex experimental setup to ensure the sample holders could maintain sample stability while

withstanding the xenon gas at high pressure. The aim of this work is to develop and utilize an aqueous barium chloride ($BaCl_2$) solution as a contrast fluid to enhance small-scale features such as mineral textures and changes in surface topology that are typically unobservable in XCT imaging. Here, XCT images of a dry Bentheimer sandstone core and the core saturated with an aqueous contrast agent are captured, qualitatively processed, and compared. The viability of use of the aqueous barium chloride contrast agent is then discussed.

3.2 Materials and Methods

3.2.1 Bentheimer Sandstone Sample

A Bentheimer sandstone sample obtained from Kocurek Industries was selected for this work. X-ray diffraction (XRD) analysis was completed by Kocurek Industries and evaluated in literature by Klein et al. (2003), Salek et al. (2022), and Asadi & Beckingham (2022). Table 3.1 indicates this sample is predominantly quartz (94.4%) with minimal amounts of albite (1.2%), K-feldspar (1.2%), and calcite (0.5%).

Table 3.1. Mineral composition of Bentheimer sample from XRD analysis (wt%).

Sample/mineral	Quartz	Albite	K-feldspar	Calcite
Bentheimer	94.4	1.2	1.2	0.5

The core sample selected for this work was 25 mm in length and 10 mm in diameter and was used for 3D x-ray computed tomography (XCT) imaging. An Anycubic Photon M3 Max Resin 3D Printer at Auburn University was used to print a resin core holder fitted for the sample. The resin core holder was designed for the sandstone core used in this work to ensure the core and aqueous contrast solution would not move during XCT imaging.

3.2.2 Contrast Agent Development

3.2.2.1 X-ray Attenuation

XCT images are often 16-bit greyscale images with voxel intensities ranging from 0 to 65,536. When a voxel has an intensity of 0 it appears as black and when a voxel has an intensity of 65,536 it appears white, while all other voxel intensities appear as shades in between. Voxel intensities in XCT images are influenced by the x-ray beams energy and by the composition and electron density of the imaged material. Materials with higher electron densities will attenuate more photons from the x-ray beam thus appearing brighter, while materials with lower electron densities will transmit more of the x-ray beams photons and appear darker (Kinahan et al., 2003).

In the XCT images collected for the dry Bentheimer sandstone sample, air filled pores have the lowest voxel intensity and appear the darkest in the image, while the minerals appear as shades of grey. When considering the minerals present in the Bentheimer sandstone, minerals containing higher electron densities such as calcite, albite, and K-feldspar will appear brighter than minerals containing lower electron densities such as quartz. However, larger x-ray beam energies are needed to image geologic porous media due to the overall density of the material. With the use of larger x-ray beam energies, the greyscale variations due to electron densities quickly converge making it difficult to segment pores and minerals within the samples. Figure 3.1 shows the x-ray attenuation based on the mass attenuation coefficients of the minerals present within the Bentheimer sandstone sample.

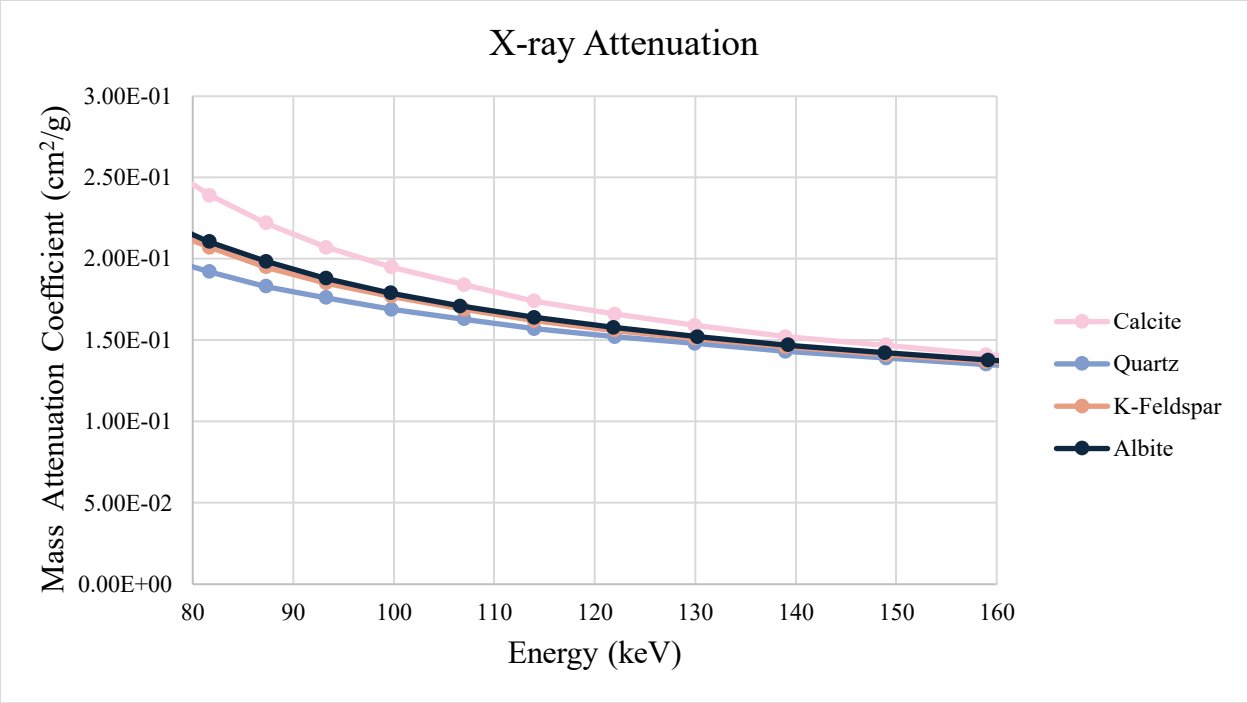

Figure 3.1. X-ray attenuation of the minerals present within the Bentheimer sample.

3.2.2.2 Contrast Agent Selection and Preparation

To enhance contrast between pores and fine details of minerals such as surface textures barium chloride was selected as a contrast agent of interest. Barium chloride was selected for this work because it is a water-soluble salt that has a higher electron density than all minerals present within the Bentheimer sandstone sample. Figure 3.2 shows the x-ray attenuation based on the mass attenuation coefficients of barium chloride, water, and all minerals present within the Bentheimer sandstone.

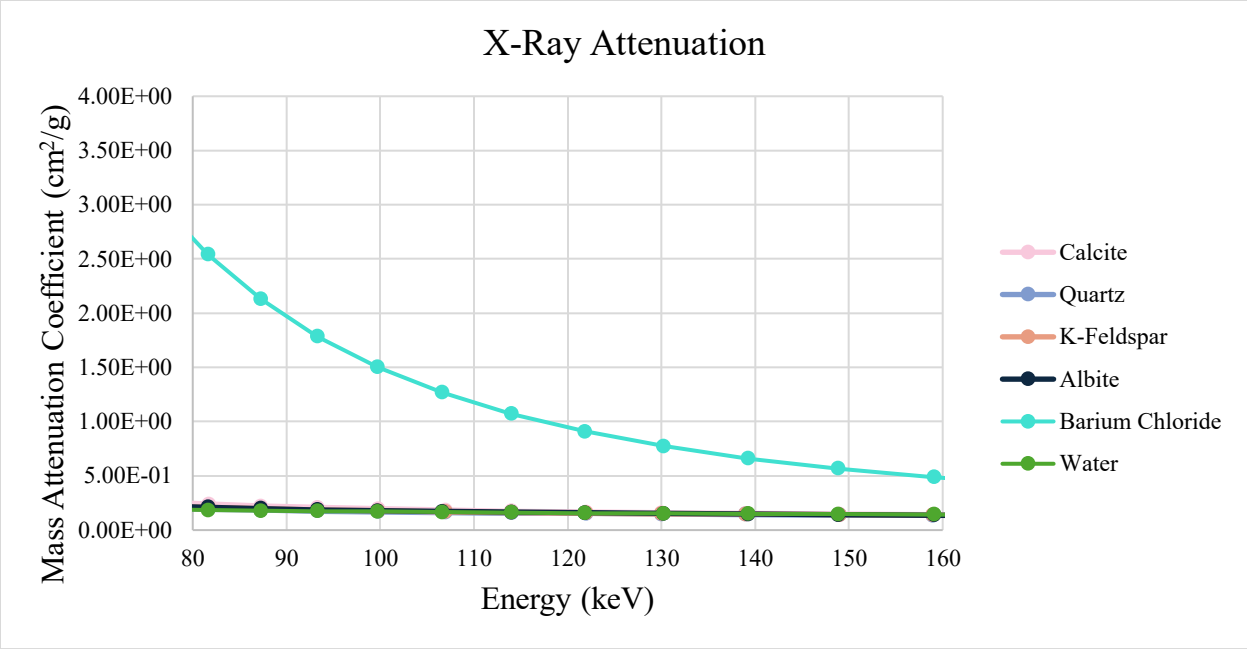

Figure 3.2. X-ray attenuation of barium chloride, water, and the minerals present within the Bentheimer sample.

Due to water having an x-ray attenuation similar to the minerals present within the sandstone sample, the contrast agent needed a high concentration of $BaCl_2$ to ensure the dissolved salt would increase the attenuation of the water. Barium chloride has a solubility of 9.5 g / 25 g H_2O at 25°C (Lide, 2007). However, only 7.8022 g were used in the creation of the contrast agent to ensure the salt would remain fully dissolved. Equations 1 and 2 were used to find the concentration of the resulting barium chloride solution:

$$\text{moles} = \frac{7.8022\ \text{g}\ BaCl_2}{208.23 \frac{\text{g}}{\text{mol}}} = 0.0375\ \text{moles}\ BaCl_2 \qquad (1)$$

$$\text{M} = \frac{7.8022\ \text{g}\ BaCl_2}{25\ \text{mL}\ H_2O} = \frac{0.0375\ \text{moles}\ BaCl_2}{0.025\ \text{L}\ H_2O} = 1.5\ \text{M} \qquad (2)$$

To create the aqueous contrast agent, 7.8022 grams of barium chloride were dissolved in 25 mL of DI water. The resulting solution had a concentration of 1.5 M and a pH of 7.77. The aqueous

barium chloride solution was added dropwise to the core holder containing the Bentheimer sandstone sample after XCT image acquisition of the dry sandstone sample. The sample holder was not removed from the Zeiss Xradia 620 Versa XCT for the addition of the contrast agent to ensure that the sample did not move between image acquisition of the dry sample and the saturated sample. After dropwise addition of the aqueous $BaCl_2$ contrast agent, the sample sat overnight to allow for the contrast agent to fill as many pores as possible before the saturated scan was obtained.

3.2.3 3D X-ray CT

3.2.3.1 Image Acquisition

A Zeiss Xradia 620 Versa XCT at Auburn University was used to obtain 996 x-y image slices images over a 360° rotation of both the dry core sample and the core sample saturated with the aqueous $BaCl_2$ solution. A voltage of 120 kV and an exposure time of 2 seconds were used to capture both sets of images with voxel resolutions of 2.945 μm. From both sets of 996 captured images, 896 slices were selected for further analysis in this work. The extracted images for the dry core sample and the core sample saturated with the aqueous $BaCl_2$ solution were registered using Dragonfly, an image processing software by Zeiss, to ensure all images aligned seamlessly and covered the same field of view. The registered images were then cropped into 1.77 mm x 1.77 mm squares with 600 pixels x 600 pixels. Both squares had total volumes of 8.24 mm^3. The images were then stacked to reconstruct the 3D images of both the dry core and the saturated core.

3.2.3.2 Image Processing

Following XCT image reconstruction of both the dry core and the saturated core, the image stacks were then filtered separately using the anisotropic diffusion filter. This filter was used to reduce noise within the images while preserving the edges of important features. The filtered dry core image stack was then manually thresholded using the Dragonfly software to separate the pore

and grain voxels. The filtered saturated core image stack was also manually thresholded using the Dragonfly software to separate the grain, $BaCl_2$ contrast agent, and the air bubble voxels. Segmentation of the grain and $BaCl_2$ contrast agent voxels was challenging due to some minerals becoming fully saturated in the contrast agent. The minerals that presented this challenge were ones observed in the dry core images having fracture like features. It is believed that due to the fracture like features the minerals became more saturated than others and thus appeared a brighter grey color closer to that of the contrast agent. Based on the SEM BSE and EDS analysis of the Bentheimer sandstone sample presented in Salek et al. (2022) it is believed that the minerals with the fracture like features are either K-feldspar or kaolinite. The porosities of the reconstructed 3D dry and saturated core samples were then calculated by counting the grain voxels of the thresholded image stacks using Dragonfly. Both image stacks were also placed side by side and qualitatively compared.

3.3 Results

3.3.1 XCT Image Acquisition and Thresholding

The reconstructed XCT images of the dry core sample can be found in Figure 3.3a. Figure 3.3b shows the thresholded XCT images of the dry core sample with pores in black and grains in white. The porosity for the dry sample was calculated by counting the number of pore and grain voxels using the Dragonfly software and was calculated to be 22.22%. The porosity calculated from the XCT images was slightly lower but agrees relatively well with the porosity of 24% provided by Kocurek Industries.

The reconstructed XCT images of the saturated core sample can be found in Figure 3.4a. The saturated core XCT images were manually thresholded to separate grain, $BaCl_2$ contrast agent, and air bubble voxels. Figure 3.4b shows the segmented XCT images of the saturated core sample with

grains in white, the $BaCl_2$ contrast agent in blue, and the air bubbles in green. The porosity for the saturated sample was calculated by counting the number of grain voxels using the Dragonfly software and was calculated to be 19.78%. The porosity calculated from the saturated core XCT images was lower than both the porosity obtained from the dry core XCT images (22.22%) and the porosity provided by Kocurek Industries (24%). This discrepancy is believed to be due to the challenges segmenting the contrast agent from the minerals believed to be K-feldspar or kaolinite. These minerals appeared brighter than other mineral phases within the sample, but not as bright as the contrast agent fluid.

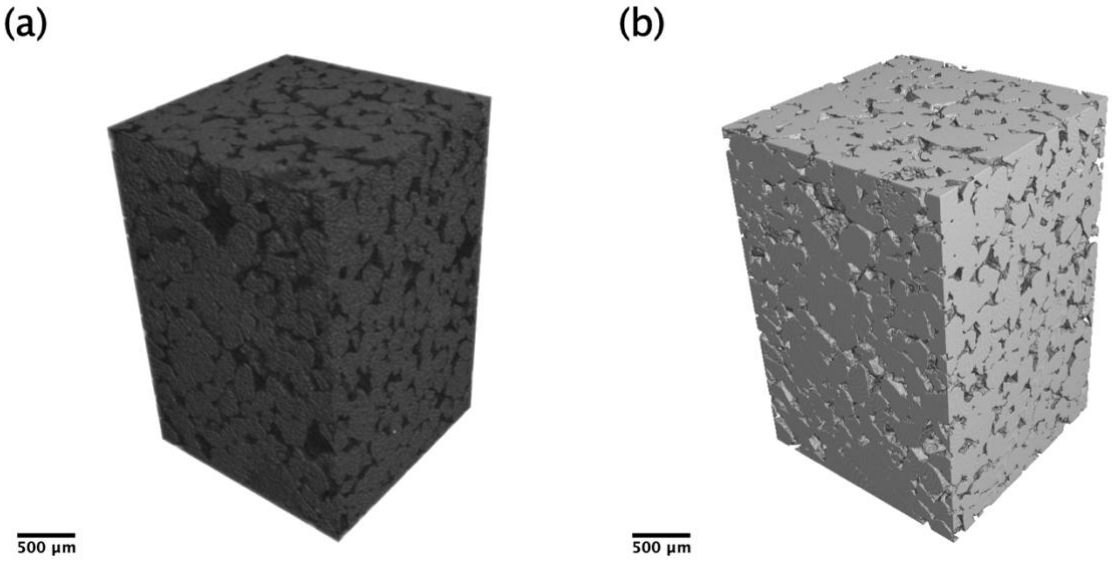

Figure 3.3. (a) Dry sandstone core reconstructed 3D XCT image stack. **(b)** Dry sandstone core thresholded 3D XCT image stack where grains are depicted in white and pores in black.

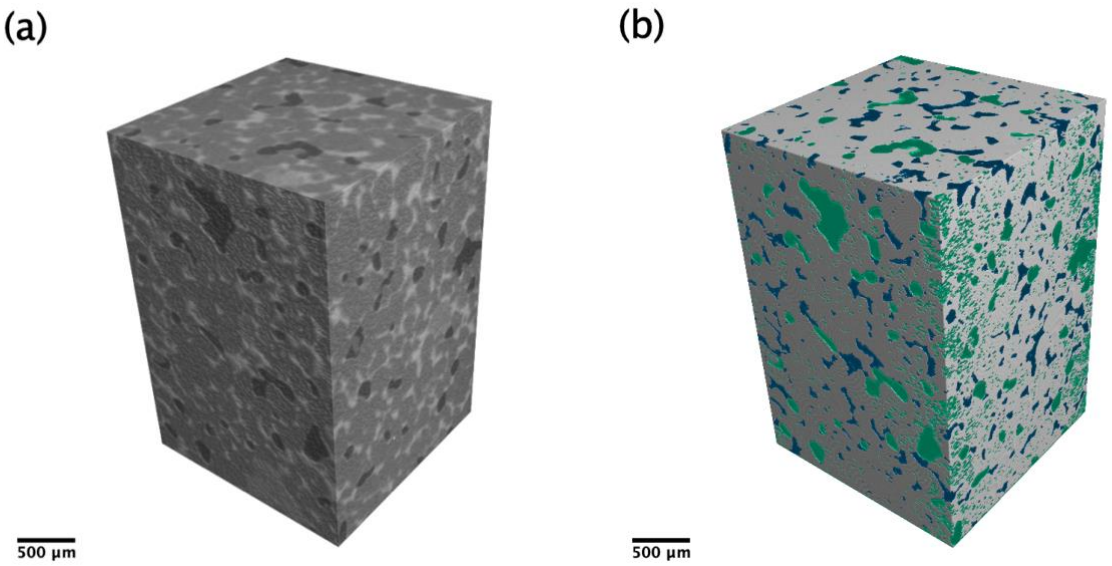

Figure 3.4. (a) Saturated sandstone core reconstructed 3D XCT image stack. **(b)** Saturated sandstone core segmented 3D XCT image stack where grains are depicted in white, the $BaCl_2$ contrast agent in blue, and the air bubbles in green.

3.3.2 XCT Image Comparison

The reconstructed 3D XCT images for both the dry core and the core saturated with the barium chloride contrast agent revealed that it was possible to increase the attenuation of pores by using an aqueous contrast agent. Overall, the XCT images for the dry core had average voxel intensities that were lower than those observed in the saturated core images. The XCT images for the saturated core appeared brighter with many pores filled with the contrast agent. However, many air bubbles are also observed in the saturated core images. Due to the presence of the air bubbles, it was difficult to determine if the pores were filled with air and inaccessible by the aqueous contrast agent or if they were connected but filled with air bubbles present in the fluid.

3.4 Discussion

As stated previously, the porosity of the Bentheimer sandstone sample provided by Kocurek Industries is 24%. However, while analyzing the dry core XCT images, a porosity of 22.22% was found. The porosity obtained from the dry core XCT images agrees well with the porosity provided

by Kocurek Industries. It is believed that the porosity obtained from the XCT images is slightly lower due to the resolution of XCT imaging unable to provide visibility of potential trace clay minerals present within the sample. The porosity was also obtained after saturating the sample in the $BaCl_2$ contrast agent. This porosity resulted as 19.78%. The drop in porosity from the unsaturated to the saturated results can potentially be due to the contrast agent increasing the attenuation of either K-feldspar or kaolinite present within the sample. When viewing the dry core XCT images some minerals have fracture like features present, but when viewing the saturated core XCT images it appears that these fracture-like features were filled with the contrast agent thus increasing the attenuation of the K-feldspar or kaolinite.

Segmentation of some minerals observed in the saturated core XCT images proved challenging. The minerals that presented the most challenge were those that appeared to have fracture like features in the dry core XCT images. It is believed that these fracture-like features were accessible by the contrast agent and caused an increase of the mineral's overall voxel intensity. As stated earlier it is believed that these minerals are either K-feldspar or kaolinite. Further research can be conducted on quantifying the connectivity of these two minerals based on their changes in x-ray attenuation with the addition of the $BaCl_2$ contrast agent. It is believed that these K-feldspar or kaolinite minerals will present greyscale values closer to the $BaCl_2$ contrast agent filled macro pores when the minerals have higher connectivity and will present greyscale values closer to the non-fractured minerals greyscale values when having lower connectivity.

Air bubbles were also observed in the saturated scan XCT images. However, it is unknown whether these bubbles were observed due to inaccessible pores containing air or if they were observed due to air bubbles being present within the aqueous contrast agent. The air bubbles were segmented during the segmentation process and while their presence is non ideal, they can still

provide valuable insights about the sample. These air bubbles were easier to segment the pore grain interfaces due to a larger difference in x-ray attenuation. It is believed that with further research these air bubbles can be used to highlight mineral boundaries and surface features typically missed during XCT imaging.

With all the information gathered from the XCT images one major difficulty arose. Due to the $BaCl_2$ contrast agent in the saturated core, it proved difficult to truly segment all minerals from the contrast agent due to the fluid filling smaller pores within the K-feldspar or kaolinite minerals. However, the change of x-ray attenuation within the K-feldspar or kaolinite minerals could potentially allow for quantification of these minerals' connectivity from XCT imaging.

3.5 Conclusion

In this work, an aqueous barium chloride solution was developed and utilized to assess the viability of contrast agent use in XCT imaging of geologic porous media. Here, porosity and visual comparisons were made for the dry core sample and the core sample saturated in the $BaCl_2$ contrast agent. The aim of this work was to visualize small-scale features such as mineral textures and changes in surface topology within geologic samples without the destructive sample preparation typically required for visualization of these features with 2D SEM imaging.

Here, the overall impact of the addition of an aqueous contrast agent was presented and discussed. It was revealed that the addition of the $BaCl_2$ contrast agent increased the x-ray attenuation of pores within core samples. In addition, the contrast agent enhanced surface textures by filling small fracture like features observed within some minerals present in the Bentheimer sandstone sample. This caused an attenuation change to those minerals which made the segmentation process more challenging, but it is believed that this change in attenuation can be used to aid in mineral connectivity in the future. It is believed that these minerals are either K-

feldspar or kaolinite based on the comparison of the results discussed here and those presented in Salek et al. (2022). Further research can be conducted on quantifying the connectivity of the K-feldspar or kaolinite minerals based on their changes in x-ray attenuation with the addition of the $BaCl_2$ contrast agent.

Chapter 4. Conclusions and Contributions to New Knowledge

4.1 Enhanced Understanding of the Impact of Region Variation on Quantified Mineral Properties

In the first study (Chapter 2), a calcareous dolomite sample obtained from Cassville Well 1 located in Bartow County, Georgia was imaged using 2D SEM and 3D XCT imaging tools. The goal of this study was to understand how region variation in a highly heterogeneous carbonate sample impacts mineral properties such as abundance, accessibility, and accessible surface area.

BSE images with resolutions of 590.9 nm, EDS images with resolutions of 820 nm, and XCT images with resolutions of 5.075 μm were obtained for two regions close in proximity, but with differing porosities were analyzed and compared. The BSE and EDS images were segmented, registered, and used to create each regions mineral map. The mineral maps were then utilized to generate and present new data on porous media and mineral characteristics including porosity, connected porosity, abundance, and accessibility. This work is notable for being the first effort to quantify accessible mineral phases in carbonate samples. This data is critical for accurate assessment and prediction of geochemical reactions in such formations.

Here, it was found that the region with lower porosity, region 1, has large abundances of dolomite and illite/mica, while the region with higher porosity, region 2, has large abundances of dolomite, quartz, and calcite. Mineral accessibilities in both regions follow the same trends with the most abundant minerals remaining the most accessible. However, region 1 has a lower porosity and region 2 has a higher porosity indicating that overall, more minerals are accessible in regions with larger porosities. Pore connectivity determined from the imaging analysis in both regions presented with less than 2%. Typically, this method is used in sandstones that have a larger percentage of connected porosity. Due to the limited pore connectivity in carbonates or other

samples more accurate quantifications of mineral accessibilities may be achieved by considering all pores are connected.

The 3D pore connectivity was extract from XCT images for each region and combined with the mineral accessibilities obtained from the representative region's mineral maps. When assuming all minerals adjacent to pores are accessible region 1 shows dolomite as the mineral with the most accessible surface area while region 2 shows quartz, dolomite, and calcite as the minerals with the highest accessible surface areas. However, when considering mineral accessible surface areas based on pore connectivity the values in region 1 show a larger change while the values in region 2 remain relatively consistent.

Overall, the study presented in Chapter 2 provides insights on how region variability is necessary to consider in carbonate samples when assessing and predicting how a host formation will be altered when subjected to GCS. While both regions were close in proximity, they both presented different trends in mineral abundances, accessibilities, and accessible surface areas. Without considering region variability predictions may over or underestimate the viability of a carbonate reservoirs characteristics as a site for GCS. It is believed that regions with similar porosities within a carbonate sample could show similar trends if imaged and analyzed, which could lead to more accurate prediction of the viability of a carbonate reservoirs storage capacity.

4.2 New Contrast Agent to Improve Visibility of Pore Networks

In Chapter 3, a dry Benthiemer sandstone core and the core saturated in an aqueous barium chloride solution were XCT imaged. The goal of this study was to assess the viability of using barium chloride as a contrast agent to enhance the visibility of small scall features typically missed in XCT imaging such as mineral textures and changes in surface topology.

XCT images with resolutions of 2.945 μm were obtained for a dry sandstone core and for the same sandstone core but saturated with the contrast agent were qualitatively analyzed and compared. The XCT images of both the dry core and the saturated core were registered, segmented, and compared to discuss the viability of utilizing a $BaCl_2$ contrast agent during XCT imaging. This work is notable for being the first to utilize a simpler and less time-consuming approach when using a contrast agent with XCT imaging of geologic porous media. This work was successful in enhancing mineral textures and changes in topology by providing increased attenuation in K-feldspar or kaolinite minerals with fracture like features. Future work can provide new insights into quantifying mineral connectivity from XCT imaging with an aqueous barium chloride contrast agent.

Here, fracture like features were found during XCT imaging of the dry core. These features then appeared fully saturated in the XCT images of the saturated core sample indicating that these features were accessible. During segmentation of minerals, air bubbles, and the $BaCl_2$ contrast agent in the saturated core images it was noticed that the minerals with these features appeared brighter than all other minerals within the sample. However, in the dry core images all minerals appear to have the same voxel intensities. It is believed that through further research quantification of mineral connectivity can be achieved with a barium chloride contrast agent.

References

Ahr, W. M. (2011). *Geology of carbonate reservoirs: the identification, description and characterization of hydrocarbon reservoirs in carbonate rocks*. John Wiley & Sons.

Aizebeokhai, A. P. (2009). Global warming and climate change: Realities, uncertainties and measures. In *International Journal of Physical Sciences* (Vol. 4, Issue 13). http://www.academicjournals.org/IJPS

Alatrash, H., & Velledits, F. (2024). Comparing petrophysical properties and pore network characteristics of carbonate reservoir rocks using micro X-ray tomography imaging and microfacies analyses. *GEM - International Journal on Geomathematics*, *15*(1). https://doi.org/10.1007/s13137-023-00243-8

Algive, L., Békri, S., Nader, F. H., Lerat, O., & Vizika, O. (2012). Impact of diagenetic alterations on the petrophysical and multiphase flow properties of carbonate rocks using a reactive pore network modeling approach. *Oil and Gas Science and Technology*, *67*(1), 147–160. https://doi.org/10.2516/ogst/2011171

Andrew, M., Bijeljic, B., & Blunt, M. J. (2014). Pore-scale contact angle measurements at reservoir conditions using X-ray microtomography. *Advances in Water Resources*, *68*, 24–31. https://doi.org/10.1016/J.ADVWATRES.2014.02.014

Anselmetti, F. S., Luthi, S., & Eberli, G. P. (1998). Quantitative Characterization of Carbonate Pore Systems by Digital Image Analysis. *American Association of Petroleum Geologists*, *82*(10), 1815–1836.

Asadi, P., & Beckingham, L. E. (2021). Integrating machine/deep learning methods and filtering techniques for reliable mineral phase segmentation of 3d x-ray computed tomography images. *Energies*, *14*(15). https://doi.org/10.3390/en14154595

Asadi, P., & Beckingham, L. E. (2022). Intelligent framework for mineral segmentation and fluid-accessible surface area analysis in scanning electron microscopy. *Applied Geochemistry*, *143*, 105387. https://doi.org/10.1016/J.APGEOCHEM.2022.105387

Asadi, P., Salek, M. F., & Beckingham, L. E. (2024). Modeling the Spatial and Temporal Evolution of Fractured Systems with a Heterogenous Mineralogy. *ACS Earth and Space Chemistry*, *8*(6), 1133–1145. https://doi.org/10.1021/acsearthspacechem.3c00322

Bachu, S., Gunter, W. D., & Perkins, E. H. (1993). Aquifer Disposal of CO2: Hydrodynamic and Mineral Trapping. *Energy Convers. Mgmt.*, *35*, 269–279. https://doi.org/10.1016/0196-8904(94)90060-4

Beckingham, L. E., Peters, C. A., Um, W., Jones, K. W., & Lindquist, W. B. (2013). 2D and 3D imaging resolution trade-offs in quantifying pore throats for prediction of permeability. *Advances in Water Resources*, *62*, 1–12. https://doi.org/https://doi.org/10.1016/j.advwatres.2013.08.010

Beckingham, L. E., Mitnick, E. H., Steefel, C. I., Zhang, S., Voltolini, M., Swift, A. M., Yang, L., Cole, D. R., Sheets, J. M., Ajo-Franklin, J. B., DePaolo, D. J., Mito, S., & Xue, Z. (2016). Evaluation of mineral reactive surface area estimates for prediction of reactivity of a multi-mineral sediment. *Geochimica et Cosmochimica Acta*, *188*, 310–329. https://doi.org/10.1016/J.GCA.2016.05.040

Beckingham, L.E., Steefel, C.I., Swift, A.M., Voltolini, M., Yang, L., Anovitz, L.M., Sheets, J.M., Cole, D.R., Kneafsey, T.J., Mitnick, E.H., Zhang, S., (2017). Evaluation of accessible mineral surface areas for improved prediction of mineral reaction rates in porous media. Geochim. Cosmochim. Acta 205, 31-49. https://doi.org/10.1016/j.gca.2017.02.006

Blunt, M., Fayers, F. J., & Orr, F. M. (1993). Carbon dioxide in enhanced oil recovery. *Energy Conversion and Management*, *34*(9–11), 1197–1204. https://doi.org/10.1016/0196-8904(93)90069-M

Chagneau, A., Claret, F., Enzmann, F., Kersten, M., Heck, S., Madé, B., & Schäfer, T. (2015). Mineral precipitation-induced porosity reduction and its effect on transport parameters in diffusion-controlled porous media. *Geochemical Transactions*, *16*(1). https://doi.org/10.1186/s12932-015-0027-z

Cnudde, V., Boone, M., Dewanckele, J., Dierick, M., van Hoorebeke, L., & Jacobs, P. (2011). 3D characterization of sandstone by means of X-ray computed tomography. *Geosphere*, *7*(1), 54–61. https://doi.org/10.1130/GES00563.1

Dai, Z., Xu, L., Xiao, T., McPherson, B., Zhang, X., Zheng, L., Dong, S., Yang, Z., Soltanian, M. R., Yang, C., Ampomah, W., Jia, W., Yin, S., Xu, T., Bacon, D., & Viswanathan, H. (2020). Reactive chemical transport simulations of geologic carbon sequestration: Methods and applications. *Earth-Science Reviews*, *208*, 103265. https://doi.org/10.1016/J.EARSCIREV.2020.103265

de Silva, G. P. D., Ranjith, P. G., & Perera, M. S. A. (2015). Geochemical aspects of CO2 sequestration in deep saline aquifers: A review. *Fuel*, *155*, 128–143. https://doi.org/10.1016/J.FUEL.2015.03.045

Delbeke, J., Runge-Metzger, A., Slingenberg, Y., & Werksman, J. (2019). *THE PARIS AGREEMENT*.

Duda, J. R., Yost II, A. B., Long, R., Dehoratiis Jr., G., & Ogunsola, O. Y. (2010). *Carbon Dioxide Enhanced Oil Recovery Untapped Domestic Energy Supply and Long Term*

Carbon Storage Solution. https://www.netl.doe.gov/sites/default/files/netl-file/CO2_EOR_Primer.pdf

Gang, S., Jia, T., Deng, Y., Li, P., Lv, M., Xing, L., & Li, L. (2025). Pore Structure Characteristics of Carbonate Rocks and Their Influence on Permeability. *ACS Omega*, *10*(22), 22613–22626. https://doi.org/10.1021/acsomega.4c10579

Glatz, G., Castanier, L. M., & Kovscek, A. R. (2016). Visualization and Quantification of Thermally Induced Porosity Alteration of Immature Source Rock Using X-ray Computed Tomography. *Energy and Fuels*, *30*(10), 8141–8149. https://doi.org/10.1021/ACS.ENERGYFUELS.6B01430

Holloway, S. (1997). An Overview of the Underground Disposal of Carbon Dioxide. *Energy Conversion and Management*, *38*, S193–S198. https://doi.org/10.1016/S0196-8904(96)00268-3

IPCC, 2005 – Bert Metz, Ogunlade Davidson, Heleen de Coninck, Manuela Loos and Leo Meyer (Eds.) Cambridge University Press, UK. pp 431. Available from Cambridge University Press, The Edinburgh Building Shaftesbury Road, Cambridge CB2 2RU ENGLAND

Jun, Y. S., Giammar, D. E., & Werth, C. J. (2013). Impacts of geochemical reactions on geologic carbon sequestration. *Environmental Science and Technology*, *47*(1), 3–8. https://doi.org/10.1021/es3027133

Kaszuba, J. P., Janecky, D. R., & Snow, M. G. (2003). Carbon dioxide reaction processes in a model brine aquifer at 200 °C and 200 bars: implications for geologic sequestration of carbon. *Applied Geochemistry*, *18*(7), 1065–1080. https://doi.org/10.1016/S0883-2927(02)00239-1

Kaszuba, J., Yardley, B., & Andreani, M. (2013). Experimental Perspectives of Mineral Dissolution and Precipitation due to Carbon Dioxide-Water-Rock Interactions. *Reviews in Mineralogy and Geochemistry*, *77*(1), 153–188. https://doi.org/10.2138/rmg.2013.77.5

Ketzer, J. M., Iglesias, R., Einloft, S., Dullius, J., Ligabue, R., & de Lima, V. (2009). Water–rock–CO2 interactions in saline aquifers aimed for carbon dioxide storage: Experimental and numerical modeling studies of the Rio Bonito Formation (Permian), southern Brazil. *Applied Geochemistry*, *24*(5), 760–767. https://doi.org/10.1016/J.APGEOCHEM.2009.01.001

Kinahan, P. E., Hasegawa, B. H., & Beyer, T. (2003). X-ray-based attenuation correction for positron emission tomography/computed tomography scanners. *Seminars in Nuclear Medicine*, *33*(3), 166–179. https://doi.org/10.1053/SNUC.2003.127307

Klein, E., & Reuschlé, T. (2003). A Model for the Mechanical Behavior of Bentheim Sandstone in the Brittle Regime. *Pure appl. geophys.* 160, 833–849 (2003). https://doi.org/10.1007/PL00012568

Kuva, J., SammaljÄrvi, J., Parkkonen, J., Siitari-Kauppi, M., Lehtonen, M., Turpeinen, T., Timonen, J., & Voutilainen, M. (2018). Imaging connected porosity of crystalline rock by contrast agent-aided X-ray microtomography and scanning electron microscopy. *Journal of Microscopy*, *270*(1), 98–109. https://doi.org/10.1111/jmi.12661

Lal, R. (2008). Carbon sequestration. *Philosophical Transactions of the Royal Society B: Biological Sciences*, *363*(1492), 815–830. https://doi.org/https://doi.org/10.1098/rstb.2007.2185

Landrot, G., Ajo-Franklin, J.B., Yang, L., Cabrini, S., Steefel, C.I., (2012). Measurement of accessible reactive surface area in a sandstone, with application to CO2 mineralization. Chem. Geol. 318, 113-125. https://doi.org/10.1016/j.chemgeo.2012.05.010

LI, Y., KANG, Z., XUE, Z., & ZHENG, S. (2018). Theories and practices of carbonate reservoirs development in China. *Petroleum Exploration and Development*, *45*(4), 712–722. https://doi.org/10.1016/S1876-3804(18)30074-0

Li, J., Zhang, P., Lu, S., Chen, C., Xue, H., Wang, S., & Li, W. (2019). Scale-Dependent Nature of Porosity and Pore Size Distribution in Lacustrine Shales: An Investigation by BIB-SEM and X-Ray CT Methods. *Journal of Earth Science*, *30*(4), 823–833. https://doi.org/10.1007/S12583-018-0835-Z

Li, C., Wang, D., & Kong, L. (2021). Application of Machine Learning Techniques in Mineral Classification for Scanning Electron Microscopy - Energy Dispersive X-Ray Spectroscopy (SEM-EDS) Images. *Journal of Petroleum Science and Engineering*, *200*, 108178. https://doi.org/10.1016/J.PETROL.2020.108178

Lide, D. R. (2007). *CRC Handbook of Chemistry and Physics* (88th ed.). CRC Press, Taylor & Francis.

Liu, P., Wang, Z., & Zhang, Z. (2021). A New Quantitative Approach for Element-Mineral Determination Based on "eDS (Energy Dispersive Spectroscopy) Method." *Geofluids*, *2021*. https://doi.org/10.1155/2021/4023704

Liu, Q., Sun, M., Sun, X., Liu, B., Ostadhassan, M., Huang, W., Chen, X., & Pan, Z. (2023). Pore network characterization of shale reservoirs through state-of-the-art X-ray computed tomography: A review. *Gas Science and Engineering*, *113*, 204967. https://doi.org/10.1016/J.JGSCE.2023.204967

Lopez Rivera, N. V., & Beckingham, L. E. (2024). Geochemical evaluation of Washita-Fredericksburg formation as a carbon storage reservoir. *Journal of Contaminant Hydrology*, *265*, 104393. https://doi.org/10.1016/J.JCONHYD.2024.104393

Luquot, L., & Gouze, P. (2009). Experimental determination of porosity and permeability changes induced by injection of CO2 into carbonate rocks. *Chemical Geology*, *265*(1–2), 148–159. https://doi.org/10.1016/J.CHEMGEO.2009.03.028

Lyu, K., She, W., Miao, C., Chang, H., & Gu, Y. (2019). Quantitative characterization of pore morphology in hardened cement paste via SEM-BSE image analysis. *Construction and Building Materials*, *202*, 589–602. https://doi.org/10.1016/J.CONBUILDMAT.2019.01.055

Machado, A. S., de Sá Silva, A. S., de Araújo, O. M. O., Santos, R. S., Leitão, R. G., dos Anjos, M. J., de Oliveira, D. F., & Lopes, R. T. (2023). Analysis of the quality of industrialized coffee powder using the techniques of computed microtomography and x-ray fluorescence. *X-Ray Spectrometry*, *52*(6), 303–311. https://doi.org/10.1002/xrs.3326

Machado, A. S., Silva, A. S. S., Campos, G. N., Gomes, C. S., Oliveira, D. F., & Lopes, R. T. (2019). Analysis of metallic archaeological artifacts by x-ray computed microtomography technique. *Applied Radiation and Isotopes*, *151*, 274–279. https://doi.org/10.1016/J.APRADISO.2019.06.016

Marmo, R., Amodio, S., Tagliaferri, R., Ferreri, V., & Longo, G. (2005). Textural identification of carbonate rocks by image processing and neural network: Methodology proposal and examples. *Computers and Geosciences*, *31*(5), 649–659. https://doi.org/10.1016/j.cageo.2004.11.016

Mayo, S., Josh, M., Nesterets, Y., Esteban, L., Pervukhina, M., Clennell, M. ben, Maksimenko, A., & Hall, C. (2015). Quantitative micro-porosity characterization using synchrotron micro-CT and xenon K-edge subtraction in sandstones, carbonates, shales and coal. *Fuel*, *154*, 167–173. https://doi.org/10.1016/J.FUEL.2015.03.046

National Academy of Sciences. (2014). *Climate Change: Evidence and Causes.* Washington, DC: The National Academies Press. https://doi.org/10.17226/18730.

Nogues, J. P., Fitts, J. P., Celia, M. A., & Peters, C. A. (2013). Permeability evolution due to dissolution and precipitation of carbonates using reactive transport modeling in pore networks. *Water Resources Research*, *49*(9), 6006–6021. https://doi.org/10.1002/wrcr.20486

Noiriel, C., Gouze, P., & Bernard, D. (2004). Investigation of porosity and permeability effects from microstructure changes during limestone dissolution. *Geophysical Research Letters*, *31*(24), 1–4. https://doi.org/10.1029/2004GL021572

Noiriel, C., Steefel, C. I., Yang, L., & Bernard, D. (2016). Effects of pore-scale precipitation on permeability and flow. *Advances in Water Resources*, *95*, 125–137. https://doi.org/10.1016/J.ADVWATRES.2015.11.013

Noiriel, C., & Daval, D. (2017). Pore-Scale Geochemical Reactivity Associated with CO2 Storage: New Frontiers at the Fluid-Solid Interface. *Accounts of Chemical Research*, *50*(4), 759–768. https://doi.org/10.1021/acs.accounts.7b00019

Oelkers, E. H., Gislason, S. R., & Matter, J. (2008). Mineral carbonation of CO2. *Elements*, *4*(5), 333–337. https://doi.org/10.2113/gselements.4.5.333

Oldenburg, C. M., Bryant, S. L., & Nicot, J. P. (2009). Certification framework based on effective trapping for geologic carbon sequestration. *International Journal of Greenhouse Gas Control*, *3*(4), 444–457. https://doi.org/10.1016/J.IJGGC.2009.02.009

Peters, C.A., (2009). Accessibilities of reactive mineral in consolidated sedimentary rock: an imaging study of three sandstones. Chem. Geol. 265 (1-2), 198-208. https://doi.org/10.1016/j.chemgeo.2008.11.014

Preibisch, S., Saalfeld, S., & Tomancak, P. (2009). Globally optimal stitching of tiled 3D microscopic image acquisitions, *Bioinformatics*, 25(11), 1463–1465, https://doi.org/10.1093/bioinformatics/btp184

Qin, F., & Beckingham, L. E. (2019). Impact of image resolution on quantification of mineral abundances and accessible surface areas. *Chemical Geology*, *523*, 31–41. https://doi.org/10.1016/J.CHEMGEO.2019.06.004

Riestenberg, D., Pashin, J., Kath, R., & Kirksey, J. (2022). SECARB-USA Cassville #1 Stratigraphic Test Borehold Update [PowerPoint slides]. Unpublished

Ritchie, H. (2020). *Sector by sector: where do global greenhouse gas emissions come from?*. [Online Resource]. Our World in Data. https://ourworldindata.org/ghg-emissions-by-sector

Rivera, N. V. L., & Beckingham, L. E. (2025). Geochemical Assessment for Carbon Sequestration in the Conasauga Group, Northwest Georgia, USA. *Greenhouse Gases: Science and Technology*. https://doi.org/10.1002/ghg.2344

Rosenfeld, A. H., Kaarsberg, T. M., & Romm, J. (2000). Technologies to reduce carbon dioxide emissions in the next decade. *Physics Today*, *53*(11), 29–34. https://doi.org/10.1063/1.1333283

Sabo, M. S., & Beckingham, L. E. (2021). Porosity-Permeability Evolution During Simultaneous Mineral Dissolution and Precipitation. *Water Resources Research*, *57*(6). https://doi.org/10.1029/2020WR029072

Safari, H., Balcom, B. J., & Afrough, A. (2021). Characterization of pore and grain size distributions in porous geological samples – An image processing workflow. *Computers & Geosciences*, *156*, 104895. https://doi.org/10.1016/J.CAGEO.2021.104895

Saif, T., Lin, Q., Butcher, A. R., Bijeljic, B., & Blunt, M. J. (2017). Multi-scale multi-dimensional microstructure imaging of oil shale pyrolysis using X-ray micro-tomography, automated ultra-high resolution SEM, MAPS Mineralogy and FIB-SEM. *Applied Energy*, *202*, 628–647. https://doi.org/10.1016/J.APENERGY.2017.05.039

Salek, M. F., Qin, F., Asadi, P., Iloejesi, C., Brunhoeber, O., Mahmood, M., & Beckingham, L. E. (2022). Impact of Pore Connectivity on Quantification of Mineral Accessibility in Sandstone Samples. *ACS Earth and Space Chemistry*, *6*(7), 1858–1867. https://doi.org/10.1021/acsearthspacechem.2c00099

Sandalow, D., Friedmann, J., McCormick, C., & McCoy, S. (2018). *ICEF Roadmap 2018*. https://www.globalccsinstitute.com/wp-content/uploads/2020/06/JF_ICEF_DAC_Roadmap-20181207-1.pdf

Santos, T. M. P., Ferreira, C. G., Araújo, O. M. O., Machado, A. S., Silva, A. S. S., & Lopes, R. T. (2020). Methodology to analyze the marginal fit of odontological crowns through tridimensional parameters using X-ray microCT technique. *Radiation Physics and Chemistry*, *167*, 108290. https://doi.org/10.1016/J.RADPHYSCHEM.2019.04.040

Schlumberger PETROLOGY Detailed Thin Section Analysis for Unconventionals. (2021).

Seigneur, N., Mayer, K. U., & Steefel, C. I. (2019). Reactive Transport in Evolving Porous Media. *Reviews in Mineralogy and Geochemistry*, *85*(1), 197–238. https://doi.org/10.2138/rmg.2019.85.7

Siqueira, T. A., Iglesias, R. S., & Ketzer, J. M. (2017). Carbon dioxide injection in carbonate reservoirs – a review of CO2-water-rock interaction studies. In *Greenhouse Gases: Science and Technology* (Vol. 7, Issue 5, pp. 802–816). https://doi.org/10.1002/ghg.1693

Smith, M. M., Sholokhova, Y., Hao, Y., & Carroll, S. A. (2013). CO2-induced dissolution of low permeability carbonates. Part I: Characterization and experiments. *Advances in Water Resources*, *62*, 370–387. https://doi.org/10.1016/J.ADVWATRES.2013.09.008

Smith, M. M., Hao, Y., & Carroll, S. A. (2017). Development and calibration of a reactive transport model for carbonate reservoir porosity and permeability changes based on CO2 core-flood experiments. *International Journal of Greenhouse Gas Control*, *57*, 73–88. https://doi.org/10.1016/J.IJGGC.2016.12.004

Stack, A. G. (2015). Precipitation in Pores: A Geochemical Frontier. *Reviews in Mineralogy and Geochemistry*, *80*(1), 165–190. https://doi.org/10.2138/rmg.2015.80.05

Steinwinder, J., & Beckingham, L. E. (2019). Role of Pore and Pore-Throat Distributions in Controlling Permeability in Heterogeneous Mineral Dissolution and Precipitation Scenarios. *Water Resources Research*, *55*(7), 5502–5517. https://doi.org/10.1029/2019WR024793

Thomas, S. (2008). Enhanced oil recovery - An overview. *Oil and Gas Science and Technology*, *63*(1 SPEC. ISS.), 9–19. https://doi.org/10.2516/ogst:2007060

Wallace, M. (2021). *The U.S. CO 2 Enhanced Oil Recovery Survey An interim update of enhanced oil production totals and CO 2 supplies for active CO 2 EOR projects in the*

U.S. as of end-of-year 2020. https://adv-res.com/pdf/ARI-2021-EOY-2020-CO2-EOR-Survey-OCT-21-2021.pdf

Wildenschild, D., & Sheppard, A. P. (2013). X-ray imaging and analysis techniques for quantifying pore-scale structure and processes in subsurface porous medium systems. *Advances in Water Resources*, *51*, 217–246. https://doi.org/10.1016/J.ADVWATRES.2012.07.018

Xu, R., Li, R., Ma, J., He, D., & Jiang, P. (2017). Effect of Mineral Dissolution/Precipitation and CO2 Exsolution on CO2 transport in Geological Carbon Storage. *Accounts of Chemical Research*, *50*(9), 2056–2066. https://doi.org/10.1021/acs.accounts.6b00651

Yin, H., Wei, B., Shmatok, A., Yang, J., Salek, M. F., Beckingham, L., Prorok, B., Wang, J., & Lou, X. (2023). On the nanoscale oxide dispersion via in-situ atmospheric oxidation during laser powder bed fusion. *Journal of Materials Processing Technology*, *322*, 118191. https://doi.org/10.1016/J.JMATPROTEC.2023.118191

Yoro, K. O., & Daramola, M. O. (2020). CO2 emission sources, greenhouse gases, and the global warming effect. Advances in Carbon Capture: Methods, Technologies and Applications, 3–28. https://doi.org/10.1016/B978-0-12-819657-1.00001-3

Zhang, L., Soong, Y., Dilmore, R., & Lopano, C. (2015). Numerical simulation of porosity and permeability evolution of Mount Simon sandstone under geological carbon sequestration conditions. *Chemical Geology*, *403*, 1–12. https://doi.org/10.1016/J.CHEMGEO.2015.03.014

2023 Sustainability Report ExxonMobil Global Outlook. (2024). www.exxonmobil.com